

Preparation and Application of a Novel S-Scheme Nanoheterojunction Photocatalyst ($\text{LaNi}_{0.6}\text{Fe}_{0.4}\text{O}_3/\text{g-C}_3\text{N}_4$)

Kexin Zhang, Rui Wang, Xin Zhong,* and Fubin Jiang*

Cite This: *ACS Omega* 2024, 9, 28422–28436

Read Online

ACCESS |



Metrics & More



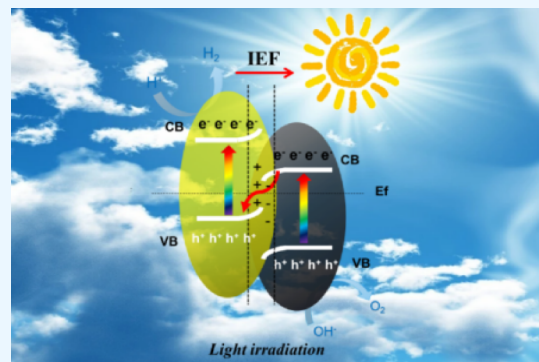
Article Recommendations



Supporting Information

ABSTRACT: Rapid recombination of photogenerated electrons and holes affects the performance of a semiconductor device and limits the efficiency of photocatalytic water splitting for hydrogen production. The use of an S-scheme nanoscale heterojunction catalyst for the separation of photo-generated charge carriers is a feasible approach to achieve high-efficiency photocatalytic hydrogen evolution. Therefore, we synthesized a three-dimensional S-scheme nanoscale heterojunction catalyst ($\text{LaNi}_{0.6}\text{Fe}_{0.4}\text{O}_3/\text{g-C}_3\text{N}_4$) and investigated its activity in photocatalytic water splitting. An analysis of the band structure (XPS, UPS, and Mott–Schottky) indicated effective interfacial charge transfer in an S-scheme nanoscale heterojunction composed of two n-type semiconductors. X-ray photoelectron spectroscopy (XPS) and electron paramagnetic resonance (EPR) spectroscopy confirmed that the light-induced charge transfer followed the S-scheme mechanism.

Based on the capture test (EPR) of $\bullet\text{OH}$ free radicals, it can be seen that the enhanced activity is attributed to the S-scheme carrier migration mechanism in heterojunction, which promotes the rapid adsorption of H^+ by the abundant amino sites in $\text{g-C}_3\text{N}_4$, thus effectively generating H_2 . The 2D/2D $\text{LaNi}_{0.6}\text{Fe}_{0.4}\text{O}_3/\text{g-C}_3\text{N}_4$ heterojunction has a good interface and produces a built-in electric field, improving the separation of e^- and h^+ while increasing the oxygen vacancy. The synergistic effect of the heterostructure and oxygen vacancy makes the photocatalyst significantly better than $\text{LaNi}_{0.6}\text{Fe}_{0.4}\text{O}_3$ and $\text{g-C}_3\text{N}_4$ in visible light. The hydrogen evolution rate of the composite catalyst ($\text{LaNi}_{0.6}\text{Fe}_{0.4}\text{O}_3/\text{g-C}_3\text{N}_4$ -70 wt %) was $34.50 \text{ mmol}\cdot\text{h}^{-1}\cdot\text{g}^{-1}$, which was 40.6 times and 9.2 times higher than that of the catalysts (LaNiO_3 and $\text{g-C}_3\text{N}_4$), respectively. After 25 h of cyclic testing, the catalyst ($\text{LaNi}_{0.6}\text{Fe}_{0.4}\text{O}_3/\text{g-C}_3\text{N}_4$ -70 wt %) composite material still exhibited excellent hydrogen evolution performance and photostability. It was confirmed that the synergistic effect between abundant active sites, enriched oxygen vacancies, and 2D/2D heterojunctions improved the photoinduced carrier separation and the light absorption efficiency of visible light. This study opens up new possibilities for the logical design of efficient photodecomposition using 2D/2D heterojunctions combined with oxygen vacancies.



1. INTRODUCTION

Photocatalytic water splitting for hydrogen production is the simplest method for converting solar energy into hydrogen energy, so it is an effective strategy for addressing the energy crisis.^{1–4} In renewable resource development, the design and synthesis of photocatalysts have garnered significant attention, and the development of efficient and cost-effective practical photocatalysts has become a crucial step. Useful photocatalysts must be environmentally friendly, devoid of heavy metals, easily prepared, and inexpensive. However, the most critical challenge lies in suppressing the rapid recombination of the photo-generated electrons and holes. Effective separation of the photogenerated electrons and holes is achieved with a built-in electric field, by band bending, or with electrostatic interactions.^{5,6} If the catalyst is designed improperly, the rapid recombination of the photogenerated electrons and holes can occur within the catalyst's interior and on the surface, thereby affecting the surface oxidation and reduction reactions of the catalyst and reducing the photocatalytic efficiency.^{7,8} Therefore, the development of catalysts with excellent activities and

stabilities is of practical significance for the sustainable utilization of green energy. In the case of traditional Z-scheme heterojunctions, specifically all-solid-state Z-scheme heterojunctions, the formation of solid-state intermediates has expanded the application scope of heterojunctions, but challenges arise in the rational design of the catalysts due to the difficulty in selecting suitable intermediates. Building upon this, we constructed an S-scheme nanoscale heterojunction in which two n-type semiconductor materials are brought into direct contact without the presence of intermediates, thus achieving rapid separation of the photogenerated electrons and holes.

Received: March 10, 2024

Revised: June 4, 2024

Accepted: June 5, 2024

Published: June 18, 2024



The perovskite structure with the general formula ABO_3 is simple and highly stable, and it exhibits excellent catalytic performance as a semiconductor photocatalyst. Within the BO_6 octahedra, the hybridization of the O 2p and transition metal 3d orbitals can induce structural distortions and changes in the oxidation state of the B-site metal, thereby altering the physicochemical properties and improving various performance aspects.^{9,10} Among perovskite-type oxides, $LaNiO_3$ material has shown promise as a photocatalyst; however, its performance requires further improvement.^{11,12} In recent years, our research group has made notable progress by exploring the use of $LaNiO_3$ as a photocatalyst for water splitting.¹³ Building upon this foundation, we hypothesized that by controlling the properties of $LaNiO_3$, we could enhance the hydrogen evolution rate of photocatalytic water splitting. Studies have shown that altering the particle sizes of the perovskites improved the catalytic activity, and the particle sizes are commonly varied through partial substitution at the B-site of the perovskite structure.^{14,15} In addition, the doped metals at the B-site generate synergism with Ni, thereby improving the catalytic performance.^{16,17} Chiba et al. doped Fe into the $LaNiO_3$ perovskite and found that $LaNi_{0.6}Fe_{0.4}O_3$ exhibited the highest stability among the $LaNi_{1-x}Fe_xO_3$ compositions. This material was more stable than $LaNiO_3$ and demonstrated higher catalytic activity in redox reactions.^{18,19} Vidal et al. also used $LaNi_{0.6}Fe_{0.4}O_3$ as a catalytic material and demonstrated its excellent conductivity and catalytic activity, and the conductivity of $751.4\text{ S}\cdot\text{cm}^{-1}$, facilitated electron transfer.^{20,21} In this study, we initially attempted to use $LaNi_{0.6}Fe_{0.4}O_3$ as a photocatalyst for water splitting and hydrogen gas evolution and achieved promising results. However, the relatively large bandgap of $LaNi_{0.6}Fe_{0.4}O_3$ limited the photocatalytic performance. To address this limitation, we hypothesized that constructing an S-scheme nanoscale heterojunction would enhance the photocatalytic activity of $LaNi_{0.6}Fe_{0.4}O_3$. g- C_3N_4 is a nonmetallic photocatalytic material, and it exhibits a broader absorption band than the common photocatalyst TiO_2 . In previous studies, we have observed the utilization of g- C_3N_4 in diverse catalytic reactions, with a notable emphasis on its application in the photocatalytic decomposition of water.²² In recent investigations into the photocatalytic decomposition of water, there has also been a proliferation of direct studies. Consequently, we hypothesize that incorporating g- C_3N_4 with perovskite materials could amplify their responsiveness to visible light.^{23–26} Additionally, the generation of an internal electric field (IEF) within the g- C_3N_4 photocatalyst has been confirmed to be an effective strategy for facilitating rapid separation of photogenerated charge carriers by guiding them toward active sites to achieve high apparent quantum efficiency (AQE) and flux. This strategy yields swift separation of the photogenerated electrons and holes.^{27–29} Based on these considerations, we employed a simple solvothermal method to fabricate a three-dimensional $LaNi_{0.6}Fe_{0.4}O_3/g-C_3N_4$ S-scheme heterojunction photocatalyst. Structural characterization of the catalyst was conducted with various techniques, including X-ray diffraction (XRD), scanning electron microscopy (SEM), transmission electron microscopy (TEM), atomic force microscopy (AFM), X-ray photoelectron spectroscopy (XPS), Fourier transform infrared spectroscopy (FT-IR), and UV–vis spectroscopy (220–800 nm). In the absence of a noble metal cocatalyst, the catalyst exhibited a high hydrogen evolution rate and excellent stability during five cycles (25 h) of testing. The catalyst ($LaNi_{0.6}Fe_{0.4}O_3/g-C_3N_4$ -70 wt %) exhibited a maximum photocatalytic activity of $34.50\text{ mmol}\cdot\text{h}^{-1}$.

g^{-1} , which was 40.6 times and 9.2 times higher than that of $LaNiO_3$ and g- C_3N_4 , respectively. In addition, this study verified that the rapid separation of the photogenerated charge carriers was confirmed with various tests such as photoluminescence spectroscopy (PL), the photocurrent response, electrochemical impedance spectroscopy (EIS), and time-resolved fluorescence spectroscopy. We gathered direct evidence of the migration pathways of the charge carriers with UV photoelectron spectroscopy, Mott–Schottky measurements, X-ray photoelectron spectroscopy, and electron paramagnetic resonance spectroscopy. This indirectly confirmed the occurrence of charge transfer in the S-scheme heterojunction and verified the formation of the built-in electric field, which facilitated band bending and the electrostatic interactions between electrons and holes. In constructing a three-dimensional nanoheterojunction, this study offers a new approach for the design and development of environmentally friendly, noble-metal-free, and highly efficient hydrogen evolution catalysts.

2. EXPERIMENTAL SECTIONS

2.1. Materials. Nickel nitrate (AR, $\geq 99.99\%$, Beijing Hulk Technology Co., Ltd.), lanthanum nitrate (AR, $\geq 99.999\%$, Beijing Hulk Technology Co., Ltd.), iron nitrate (AR, $\geq 99.99\%$, Beijing Hulk Technology Co., Ltd.), citric acid (AR, $\geq 99.5\%$, Aladdin), ultrapure water (purified using a Milli-Q purification system), anhydrous methanol (AR, $\geq 99.99\%$, Aladdin), ethanol (AR, $\geq 99.7\%$, Beijing Tong Guang Fine Chemical Co., Ltd.), and urea (AR, $\geq 99\%$, Xiong Scientific Co., Ltd.) were used in this experiment. All of the reagents were used without further purification. All experiments were conducted in deionized water with a resistivity of $18\text{ M}\Omega\cdot\text{cm}$.

2.2. Catalyst Preparation. **2.2.1. Preparation of $LaNi_{0.6}Fe_{0.4}O_3$.** By calculation, 0.8724 g of nickel nitrate, 0.8080 g of iron nitrate, 2.1651 g of lanthanum nitrate, and 1.9210 g of citric acid were dissolved in 10 mL of deionized water and 5 mL of ethanol to prepare a deep green transparent solution. The solution was maintained at a constant temperature of $80\text{ }^\circ\text{C}$ in a water bath with magnetic stirring until it reached a sol state. It was then transferred to a drying oven at $120\text{ }^\circ\text{C}$ and thoroughly dried for 10 h to obtain a solid sample in balloon form, which was subsequently finely ground. Finally, the sample was calcined in a box-type muffle furnace (ramping up at a rate of $5\text{ }^\circ\text{C}\cdot\text{min}^{-1}$ to $400\text{ }^\circ\text{C}$ and held for 4 h, followed by ramping up to $700\text{ }^\circ\text{C}$ at a rate of $5\text{ }^\circ\text{C}\cdot\text{min}^{-1}$ and maintaining at $700\text{ }^\circ\text{C}$ for 4 h).

2.2.2. Preparation of g- C_3N_4 . Dry 20 g of urea in a forced air oven at $80\text{ }^\circ\text{C}$ for 10 h and then grind it. Place the ground urea in a ceramic boat and heat it in a muffle furnace to $550\text{ }^\circ\text{C}$, maintaining this temperature for 5 h. After the product was cooled to room temperature, a yellow powder was obtained.

2.2.3. Preparation of $LaNi_{0.6}Fe_{0.4}O_3/g-C_3N_4$ Composites. A certain amount of $LaNi_{0.6}Fe_{0.4}O_3$ was dispersed in 15 mL of anhydrous ethanol and sonicated for 30 min to obtain suspension A. Simultaneously, an appropriate amount of ethanol was added dropwise to g- C_3N_4 , followed by mechanical stirring to obtain a yellow dispersion solution B. Under constant temperature conditions of $20\text{ }^\circ\text{C}$, suspension A was slowly added to solution B to obtain sample C. After 1 h of ultrasonication and 12 h of magnetic stirring, sample C was transferred to a hydrothermal reactor and heated at $120\text{ }^\circ\text{C}$ for 6 h. Following this, it underwent 5 rounds of centrifugation, followed by thorough drying for 12 h, resulting in the preparation of $LaNi_{0.6}Fe_{0.4}O_3/g-C_3N_4$ nanosheet samples with different g- C_3N_4 contents of 65, 70, and 75 wt %.

2.3. Characterization. The surface morphologies and microstructures of the samples were characterized with a scanning electron microscope (SEM, HITACHI S-4800). The crystal structures and compositions of the samples were determined with a Shimadzu Maxima X-ray diffractometer (XRD 7000) with Cu K α radiation at a current of 30 mA and voltage of 40 kV. The composition proportion of the heterojunction was proved by thermogravimetric analysis (TGA). The lattice spacings and particle growth were characterized with a transmission electron microscope (TEM, FEI Talos F200S), and the elemental distributions were analyzed with energy-dispersive spectroscopy (EDS). The formation of nanoheterostructures was confirmed by atomic force microscopy (AFM) after the samples were drip-coated onto a substrate following UV treatment. X-ray photoelectron spectroscopy (XPS) was conducted with a Thermo Fisher ESCALAB 250Xi electron spectrometer equipped with a monochromatic microfocused Al K α X-ray source, and the binding energy of the C 1s peak at 284.8 eV was used for calibration. Fourier transform infrared (FT-IR) spectroscopy was performed with a Shimadzu IRAffinity-1 infrared spectrometer. The optical properties of the prepared samples were examined with a UV-2600 spectrophotometer (Shimadzu Corporation) with BaSO $_4$ as a blank substrate for UV–vis diffuse reflectance spectroscopy (DRS). Photoluminescence spectra were recorded with an FS 980 fluorescence spectrometer at room temperature, with a 300 nm excitation wavelength provided by a 500 W xenon lamp. Time-resolved fluorescence (TRF) spectra of the samples were obtained at room temperature with a fluorescence spectrometer and 280 nm laser excitation (Quanturus-Tau, C11367, HAMAMATSU). Photovoltaic measurements were performed with a CHI1030C electrochemical workstation and a standard three-electrode system, in which a platinum mesh served as the working electrode, and a Ag/AgCl electrode was used as the reference electrode. The samples, including 5 mg of LaNi $_{0.6}$ Fe $_{0.4}$ O $_3$, g-C $_3$ N $_4$, and LaNi $_{0.6}$ Fe $_{0.4}$ O $_3$ /g-C $_3$ N $_4$ -70 wt %, were dissolved in a mixture comprising 800 μ L of distilled water, 200 μ L of isopropanol, and 30 μ L of Nafion solution to obtain a slurry, which was then sonicated and drip-cast onto a glassy carbon electrode to form the working electrode. A 500 W xenon lamp was employed as the light source, with a 5 nm excitation and emission slit width, and a 0.1 mol/L KHCO $_3$ solution was used as the electrolyte. Mott–Schottky (M-S) curves and photocurrent response curves (I-t) were generated to determine the charge carrier migration resistance by electrochemical impedance spectroscopy. A 5 mmol/L Fe (CN) $_6^{3-/4-}$ solution and 0.1 mol/L KCl solution were employed as the electrolyte. The hydrogen gas yield was determined with a Shimadzu GC-2014C gas chromatograph. Electron spin resonance spectra were measured with an electron spin resonance spectrometer (Bruker E500).

2.4. Full Spectrum Photocatalytic Decomposition of Water for Hydrogen Production. To simulate natural sunlight conditions, we used a 300 W (250–1200 nm) xenon lamp as the light source and added the target catalyst to an aqueous solution containing 20% (volume) methanol as the sacrificial reagent for testing. Maintain the temperature at 25 $^{\circ}$ C through a constant temperature device while maintaining magnetic stirring throughout the entire process. Add an appropriate amount of sample and secondary water to a 300 mL quartz round-bottom flask. After adding 20 mL of anhydrous methanol, seal and vacuum at low temperature to introduce N $_2$

for 60 min. The hydrogen production rate was recorded by gas chromatography, and each sample consisted of five parallel experiments with the entire process maintained at room temperature.

The formula for calculating the apparent quantum efficiency is as follows:

$$\text{AQY}(\%) = \frac{2 \times \text{number of evolved hydrogen molecules}}{\text{number of incident photos}} \times 100\% \quad (1)$$

3. RESULTS AND DISCUSSION

3.1. Structure and Performance. Here, we synthesized LaNi $_{0.6}$ Fe $_{0.4}$ O $_3$ and LaNi $_{0.6}$ Fe $_{0.4}$ O $_3$ /g-C $_3$ N $_4$ composites in a simple way. The synthesis process of the photocatalyst is shown in Figure S1.

The crystal structures of the prepared samples were analyzed by X-ray diffraction (XRD) patterns. The crystal structure and phase purity of the LaNi $_{0.6}$ Fe $_{0.4}$ O $_3$ powder are shown in Figure 1.

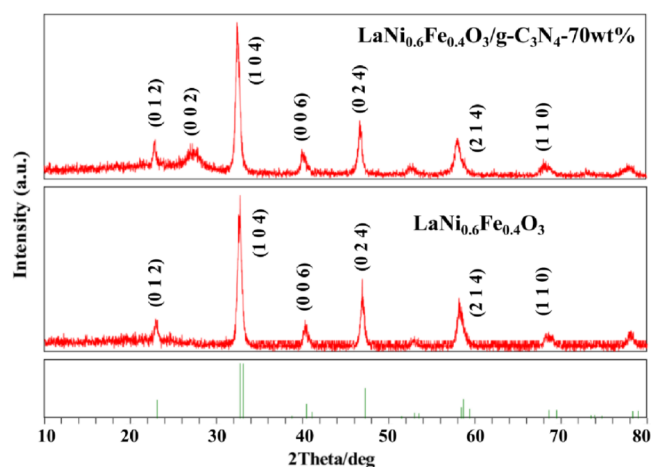


Figure 1. XRD patterns of the as-prepared LaNi $_{0.6}$ Fe $_{0.4}$ O $_3$ and LaNi $_{0.6}$ Fe $_{0.4}$ O $_3$ /g-C $_3$ N $_4$ photocatalysts.

The characteristic peaks of LaNi $_{0.6}$ Fe $_{0.4}$ O $_3$ corresponded to those reported in JCPDS card No. 88–0637 in the database. An analysis of the spectrum indicated the absence of significant impurities in the product. Due to the partial substitution of Fe for Ni, the peak intensity of the sample decreased, and the peak gradually broadened. A clear transition from the orthorhombic *Pnma* (PDF #88–0641) to the trigonal *R $\bar{3}c$* (PDF #88–0633) crystal structure was observed when the proportion of Fe reached 0.4, as in LaNi $_{0.6}$ Fe $_{0.4}$ O $_3$.³⁰ These results indicated that the lattice parameters changed, which was attributed to the different ionic radii of the cations and the resulting distortion of the Fe/Ni octahedra and lattice contraction, which neutralized the charge imbalance. Upon combining the LaNi $_{0.6}$ Fe $_{0.4}$ O $_3$ with g-C $_3$ N $_4$, a new peak for g-C $_3$ N $_4$ appears at 27.7 $^{\circ}$ (0 0 2), and the intensities of the peaks for LaNi $_{0.6}$ Fe $_{0.4}$ O $_3$ decreased significantly. This provided evidence for the successful preparation of the nanocomposite heterostructure material.²⁷ The types and contents of the catalysts were determined. The ICP test results are shown in Table 1, where Ni:Fe \approx 6:4, which verified the actual ratio between Co and Fe in LaNi $_{0.6}$ Fe $_{0.4}$ O $_3$. Other target products with doping ratios are listed in Figure S2.

Figure 2a shows that LaNi $_{0.6}$ Fe $_{0.4}$ O $_3$ contained multiple ellipsoidal particles with a uniform particle size distribution. As

Table 1. Elements in $\text{LaNi}_{0.6}\text{Fe}_{0.4}\text{O}_3/\text{g-C}_3\text{N}_4$ -70% and the Percentage Content of Each Element After Pickling

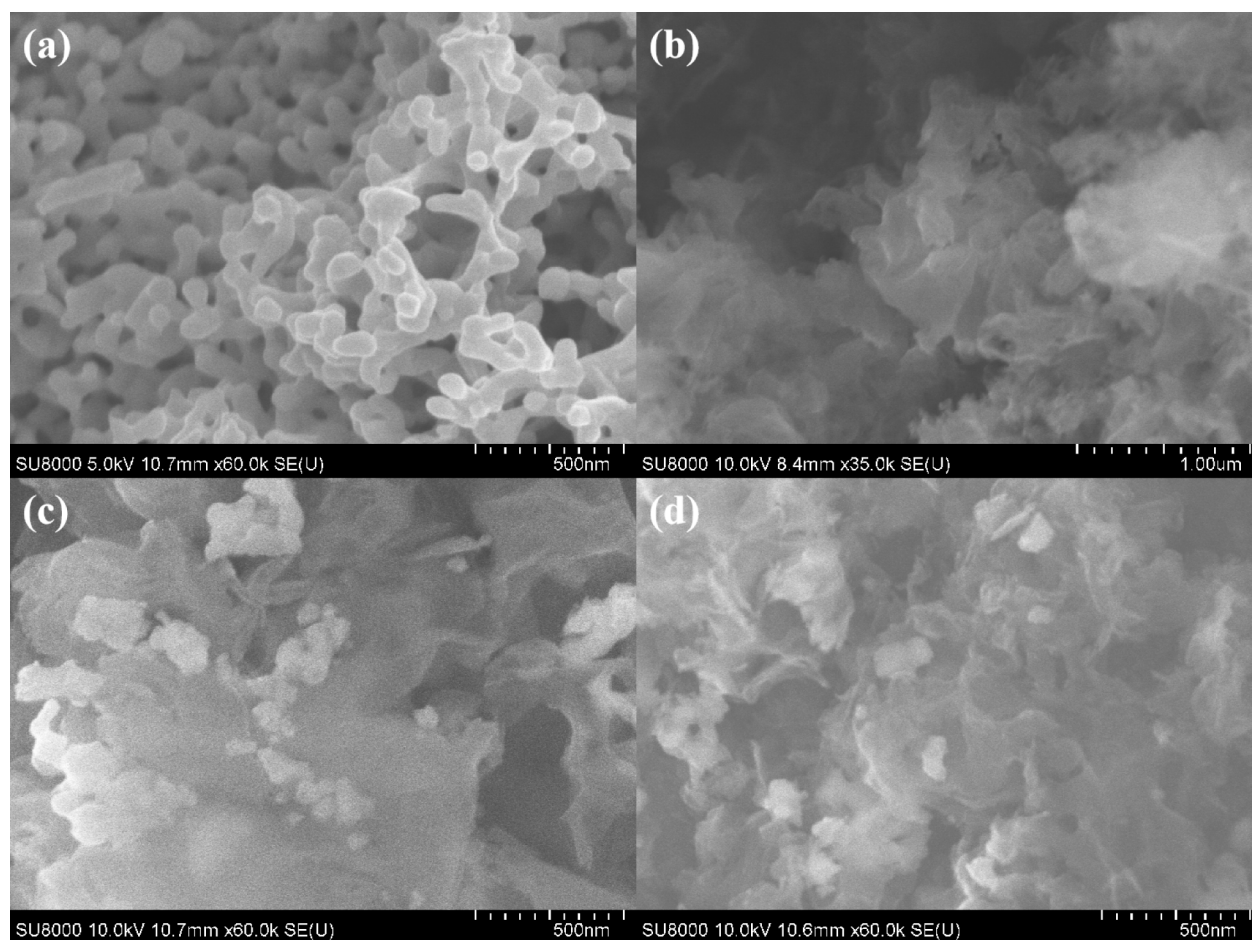
element	La	Ni	Fe	C	N
percentage content (wt %)	6.4	3.5	2.4	30.2	40.6

shown in Figure 2b–d, the $\text{LaNi}_{0.6}\text{Fe}_{0.4}\text{O}_3$ nanoparticles were dispersed on the surface of $\text{g-C}_3\text{N}_4$ in particulate form and grew in the form of clusters, forming a three-dimensional nanostructure. This staggered structure exhibited a large surface area, allowing both the surface and the interior to receive the light source, thereby increasing the number of active sites for photocatalytic hydrogen production via water splitting. The specific area, average pore size, and average particle size of the samples were measured by the BET technique. Figure S3 shows that the nitrogen adsorption analytical isotherms of $\text{LaNi}_{0.6}\text{Fe}_{0.4}\text{O}_3$ and $\text{LaNi}_{0.6}\text{Fe}_{0.4}\text{O}_3/\text{g-C}_3\text{N}_4$ are inconsistent with the desorption curves and there is a hysteresis ring. In line with the characteristics of the type IV adsorption equilibrium isotherm, all are mesoporous materials. Table S1 shows that the pore size of the sample is concentrated in the range of 2–3 nm, which belongs to mesopores, which is also consistent with the above adsorption and desorption isotherm analysis results. The specific surface areas of $\text{LaNi}_{0.6}\text{Fe}_{0.4}\text{O}_3$ and $\text{LaNi}_{0.6}\text{Fe}_{0.4}\text{O}_3/\text{g-C}_3\text{N}_4$ are 101.69 and 162.79 $\text{m}^2 \text{g}^{-1}$, respectively. The specific surface area of $\text{LaNi}_{0.6}\text{Fe}_{0.4}\text{O}_3/\text{g-C}_3\text{N}_4$ is 1.6 times that of $\text{LaNi}_{0.6}\text{Fe}_{0.4}\text{O}_3$. The combination of the two is beneficial for

increasing the number of active sites so as to improve the photocatalytic water splitting activity.

TEM and HRTEM were used to determine the morphology, elemental composition, structural composition, and particle sizes of the catalyst, and their impacts on the catalytic performance were investigated. As shown in Figure 3a, $\text{LaNi}_{0.6}\text{Fe}_{0.4}\text{O}_3$ exhibited distinct elliptical particles with sizes of 60–70 nm. In Figure 3b, well-crystallized $\text{LaNi}_{0.6}\text{Fe}_{0.4}\text{O}_3$ nanoparticles are observed with clear lattice spacings (d -spacings), and the distances between the adjacent lattice fringes are consistent. The interplanar spacing of approximately 0.272 nm corresponded to the crystal plane (1 0 4). The $\text{g-C}_3\text{N}_4$ exhibited a layered structure, with $\text{LaNi}_{0.6}\text{Fe}_{0.4}\text{O}_3$ nanoparticles dispersed on the surface, consistent with the images in Figure 3c. Lattice plane separation was observed at the interface, as in Figure 3d,e, the interplanar spacing of approximately 0.27 nm indicated the (1 0 4) planes. The crystal plane indexes (1 0 4) and (1 1 0) obtained from the XRD data correspond to the distinct diffraction peaks (2.70Å and 3.65Å) in the SAED pattern, as shown in Figure 3f. Figure 3g presents energy-dispersive X-ray spectroscopy (EDS) data, which confirmed the elemental composition of $\text{LaNi}_{0.6}\text{Fe}_{0.4}\text{O}_3$ and the absence of other elements. The elements La, Ni, Fe, C, N, and O were uniformly distributed in the $\text{LaNi}_{0.6}\text{Fe}_{0.4}\text{O}_3/\text{g-C}_3\text{N}_4$ -70 wt % catalyst.

The atomic force microscopy (AFM) images enabled high-resolution visualization of the micronano surface morphology, as

**Figure 2.** SEM images of (a) $\text{LaNi}_{0.6}\text{Fe}_{0.4}\text{O}_3$, (b) $\text{g-C}_3\text{N}_4$, and (c, d) $\text{LaNi}_{0.6}\text{Fe}_{0.4}\text{O}_3/\text{g-C}_3\text{N}_4$ -70 wt % composites.

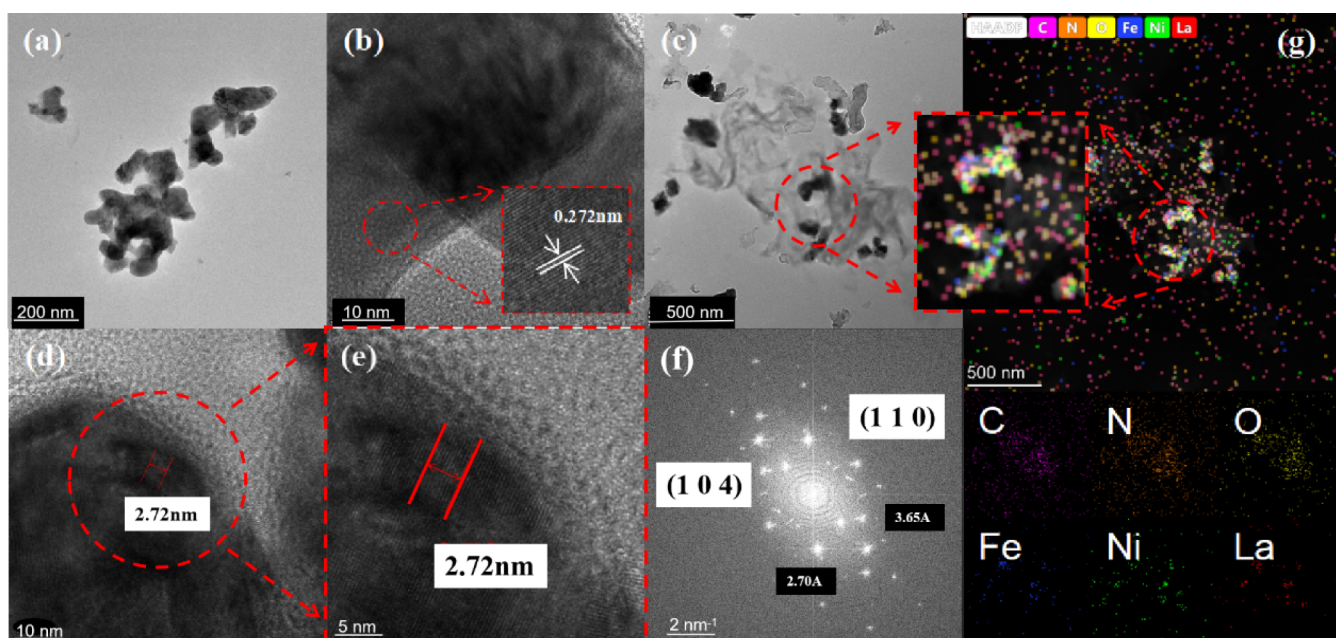


Figure 3. (a) TEM image and (b) HRTEM image of LaNi_{0.6}Fe_{0.4}O₃; (c) TEM image, (d,e) high-magnification TEM images, and (f) selected area electron diffraction (SAED) pattern of LaNi_{0.6}Fe_{0.4}O₃/g-C₃N₄-70 wt %; (g) SEM image of LaNi_{0.6}Fe_{0.4}O₃/g-C₃N₄-70 wt % and energy-dispersive X-ray (EDS) images showing the C, N, O, Fe, Ni, and elemental distribution.

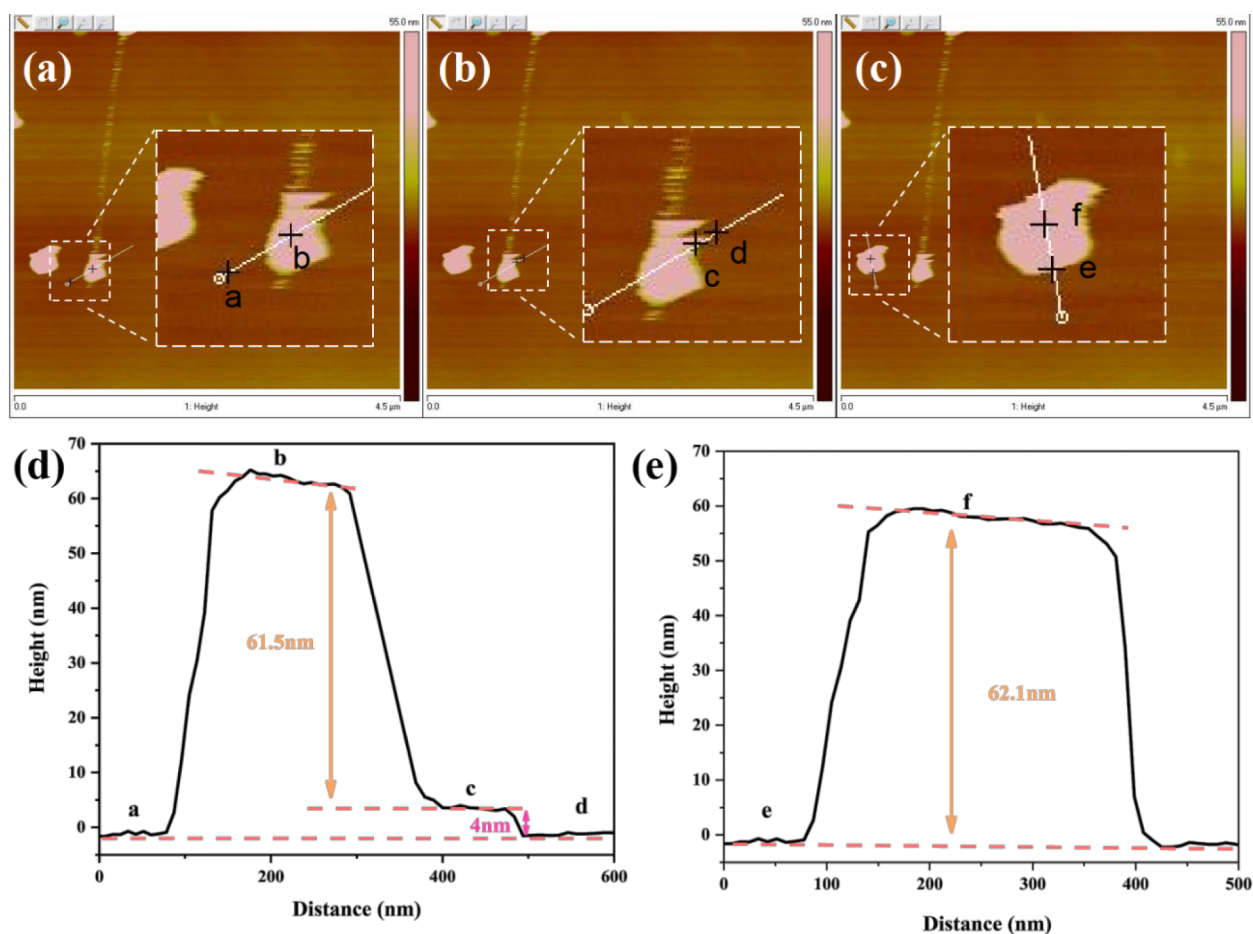


Figure 4. (a–c) AFM image and (d, e) profile image of the LaNi_{0.6}Fe_{0.4}O₃/g-C₃N₄-70 wt %.

shown in Figure 4. Brighter regions in the image corresponded to greater surface heights, while the darker regions represented

flatter surface sections, and the color scale is located on the right side of the image. The AFM image shows the overall topography

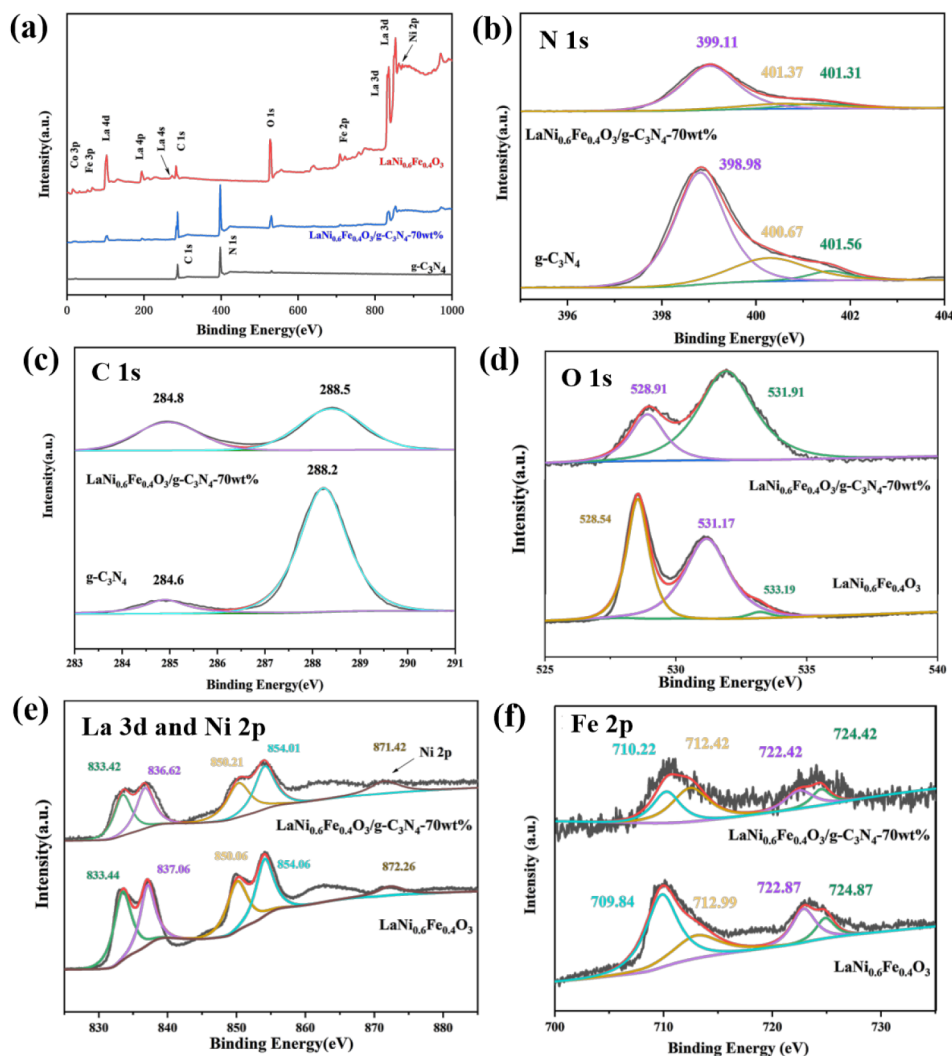


Figure 5. X-ray photoelectron spectroscopy (XPS) full spectrum. (a) and (b) N 1s; (c) C 1s; (d) O 1s; (e) La 3d and Ni 2p, and (f) Fe 2p magnified high-resolution spectra for $\text{LaNi}_{0.6}\text{Fe}_{0.4}\text{O}_3$, $\text{g-C}_3\text{N}_4$, and $\text{LaNi}_{0.6}\text{Fe}_{0.4}\text{O}_3/\text{g-C}_3\text{N}_4$ -70 wt %.

Table 2. XPS Binding Energy of $\text{LaNi}_{0.6}\text{Fe}_{0.4}\text{O}_3$, $\text{g-C}_3\text{N}_4$, and $\text{LaNi}_{0.6}\text{Fe}_{0.4}\text{O}_3/\text{g-C}_3\text{N}_4$ -70 wt %

	Ni 2p	Fe 2p		O 1s
		Fe 2p _{3/2}	Fe 2p _{1/2}	
$\text{LaNi}_{0.6}\text{Fe}_{0.4}\text{O}_3$	770.3	709.8	722.8	531.9 (47%)
	771.7	712.9	724.8	
$\text{LaNi}_{0.6}\text{Fe}_{0.4}\text{O}_3/\text{g-C}_3\text{N}_4$ -70 wt %	772.3	710.2	722.4	531.3 (62%)
	772.8	712.4	724.4	

of the scanned area, and the height distribution curves were extracted for specific locations. The black height curves in the image correspond to the height distribution at the positions indicated by the black lines in the AFM image. With the AFM data, we observed a well-grown nanoheterostructured catalyst ($\text{LaNi}_{0.6}\text{Fe}_{0.4}\text{O}_3/\text{g-C}_3\text{N}_4$ -70 wt %). Spherical $\text{LaNi}_{0.6}\text{Fe}_{0.4}\text{O}_3$ nanoparticles were found to grow steadily on the layered $\text{g-C}_3\text{N}_4$ substrate, with heights measuring approximately 61.5 and 4 nm, respectively. This observation was consistent with the SEM and TEM data, confirming that the prepared $\text{g-C}_3\text{N}_4$ was a suitable substrate. The AFM images provided valuable insights into the morphology and height distribution of the catalyst and contributed to a comprehensive understanding of the micro-nano structure.

We determined the surface elemental chemical states with X-ray photoelectron spectroscopy (XPS), as shown in Figure 5. The C 1s peak was corrected to a binding energy of 284.8 eV. The $\text{LaNi}_{0.6}\text{Fe}_{0.4}\text{O}_3/\text{g-C}_3\text{N}_4$ -70 wt % composite material consisted of La, Ni, Fe, O, C, and N elements. The high-resolution N 1s spectrum of the $\text{g-C}_3\text{N}_4$ sample, shown in Figure 5b, can be divided into three major peaks at 399.1, 400.7, and 401.6 eV. The main peak at 399.1 eV is attributed to the sp^2 -hybridized nitrogen (C—N=C) of the heptazine-triazine ring, while the peaks located at 400.7 and 401.6 eV correspond to the tertiary nitrogen N—(C)₃ groups and surface amino functions (C—N—H). After the formation of heterojunction, the amino group increases, increasing the active site.⁴³ In the high-resolution Fe 2p spectrum shown in Figure 5f, there were two

shoulder peaks at 709.84 and 712.99 eV, 722.87 and 724.87 eV, which corresponded to the binding energies of the Fe 2p_{3/2} and Fe 2p_{5/2} states, respectively. After doping with Fe, the proportion of M²⁺/M³⁺ increased, which enriched the oxygen vacancies (OVs) and inhibited direct electron–hole recombination (Table 2).^{30,31} The high-resolution O 1s XPS data contained two main peaks near 528.54 and 531.17 eV, as shown in Figure 5d. The spectrum of the pure LaNi_{0.6}Fe_{0.4}O₃ sample was deconvoluted into three peaks: the peak with the lowest binding energy (approximately 528.54 eV) was due to the lattice oxygen atoms on the surface; the next peak (approximately 531.17 eV) was due to the adsorbed oxygen on the surface; and the peak with the highest binding energy (approximately 533.19 eV) was due to the adsorption of water. The high-resolution O 1s spectrum of LaNi_{0.6}Fe_{0.4}O₃/g-C₃N₄-70 wt % exhibited two main peaks at 528.91 and 531.91 eV, which were attributed to surface lattice oxygen atoms and surface adsorbed oxygen, respectively.³¹ The peak positions for the surface adsorbed oxygens in the LaNi_{0.6}Fe_{0.4}O₃/g-C₃N₄-70 wt % spectrum increased by 0.7 eV, and the peak areas were increased, indicating that the adsorbed oxygen content in LaNi_{0.6}Fe_{0.4}O₃/g-C₃N₄ was significantly increased after binding of the g-C₃N₄ with LaNi_{0.6}Fe_{0.4}O₃. The less obvious characteristic peak of Ni 2p is located at 770 eV.^{32,33} The La 3d spectrum shown in Figure 5e for the LaNi_{0.6}Fe_{0.4}O₃/g-C₃N₄ sample exhibited two shoulder peaks with vibrational features in the binding energy ranges of 833–837 eV and 850–854 eV. These shoulder peaks were split into two distinct peaks at 833.44 and 837.06 eV, and at 850.06 and 854.06 eV, which corresponded to the binding energies of La 3d_{5/2} and La 3d_{3/2}, respectively. This confirmed the presence of La³⁺ ions in the crystal structure.³⁴

The Fourier transform infrared (FT-IR) spectra of LaNi_{0.6}Fe_{0.4}O₃, LaNi_{0.6}Fe_{0.4}O₃/g-C₃N₄-70 wt %, and g-C₃N₄ are shown in Figure 6. For pure g-C₃N₄, the characteristic peaks

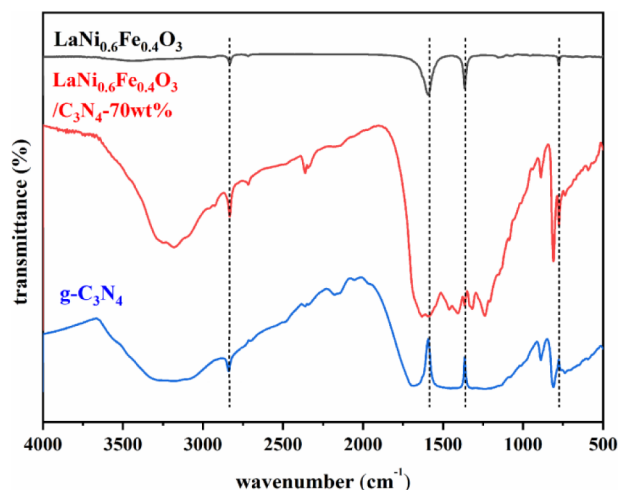


Figure 6. Fourier transform infrared (FT-IR) spectra of g-C₃N₄, LaNi_{0.6}Fe_{0.4}O₃, and LaNi_{0.6}Fe_{0.4}O₃/g-C₃N₄-70 wt %.

at 1508.4 cm⁻¹, 1541.2 cm⁻¹, and 1558.6 cm⁻¹ corresponded to the stretching vibrational modes of the aromatic CN groups. Another characteristic absorption peak appeared at 810 cm⁻¹, which corresponded to the vibrational modes of g-C₃N₄ (triazine units) and surface N–H groups. In the 2000–400 cm⁻¹ region of the FT-IR spectrum, only two obvious absorption bands were observed for LaNi_{0.6}Fe_{0.4}O₃. The vibration peaks at 700 and 760 cm⁻¹ arose from the Ni–O

bending and tensile vibrations of the perovskite structure. The peak splitting was attributed to the Jahn–Teller effect of Ni³⁺, which caused local deformation in the lattice.¹¹ With increasing g-C₃N₄ content in the LaNi_{0.6}Fe_{0.4}O₃ sample, the characteristic peak for the composite material gradually becomes sharper. The distinct and sharp peak at around 807 cm⁻¹ was originated from representative tri-s-triazine units. In addition, compared with the spectrum of g-C₃N₄, the spectrum of the LaNi_{0.6}Fe_{0.4}O₃/g-C₃N₄ sample showed a blueshift to 810 cm⁻¹ for the triazine units.²⁸ This indicated a decrease in the number of hydrogen bonds in the g-C₃N₄ structure, which could facilitate the transfer of charge carriers in the g-C₃N₄.

Prior research has shown that the electronic bandgap energy of a material determines its photocatalytic activity. Studying the positions of the conduction band (CB) and valence band (VB) of the sample is also of great significance for understanding the mechanism of photocatalytic decomposition of water and hydrogen evolution. In most cases, E_{CB} can obtain approximate flat band values through Mott–Schottky curve measurements, but even such approximations are not very accurate. In combination with the bandgap graph obtained from the Kubelka–Munk function, the E_{VB} is easily derived. As shown in Figure 7a, the solid UV diffuse reflectance spectra of pure LaNi_{0.6}Fe_{0.4}O₃, g-C₃N₄, and LaNi_{0.6}Fe_{0.4}O₃/g-C₃N₄ were measured by using a solid UV diffuse reflectance spectrum. The LaNi_{0.6}Fe_{0.4}O₃/g-C₃N₄ composite material exhibited absorption properties similar to g-C₃N₄ and LaNi_{0.6}Fe_{0.4}O₃ absorbed light in almost all cases, indicating that the LaNi_{0.6}Fe_{0.4}O₃ has excellent photoelectric properties. The absorption edge of the LaNi_{0.6}Fe_{0.4}O₃/g-C₃N₄ composite material was red-shifted compared to that of pure g-C₃N₄, indicating that the LaNi_{0.6}Fe_{0.4}O₃/g-C₃N₄ composite material can absorb more visible light. The bandgap energy of a semiconductor is as follows:

$$(ah\nu)^{1/n} = A(h\nu - E_g) \quad (2)$$

where α , h , ν , A , E_g , and n represent the absorption coefficient, Planck's constant, incident light frequency, constant, the bandgap, and an integer, respectively. Figure 7b reveals that the bandgap energies (E_g) of LaNi_{0.6}Fe_{0.4}O₃ and LaNi_{0.6}Fe_{0.4}O₃/g-C₃N₄ were approximately 2.65 and 1.93 eV, respectively. The composite material exhibited a smaller bandgap energy (E_g) value. The valence band (VB) and conduction band (CB) energies of semiconductors can also be obtained with the following empirical formulas:

$$E_{CB} = \chi - E^\theta - 0.5E_g \quad (3)$$

$$E_{VB} = E_{CB} + E_g \quad (4)$$

According to the literature, the values for pure LaNi_{0.6}Fe_{0.4}O₃ and g-C₃N₄ are approximately 6.60 and 4.63 eV, respectively.³⁰ E^θ is the energy of free electrons (approximately 4.5 eV relative to NHE), and E_g is the bandgap energy of the semiconductor. As shown in Figure 7c,d, the positive slope of the M–S plot indicates that LaNi_{0.6}Fe_{0.4}O₃ is a typical n-type semiconductor.³⁵ To ensure accuracy, we also tested the parameters at 2000 and 3000 Hz, as shown in Figure S4. Figure 7e verified that the numerical value of E_{VB} matched that of the Kubelka–Munk function calculation.

Table 3 shows the calculated values for the E_{CB} and E_{VB} . The results show that the E_{CB} of g-C₃N₄ (−1.42 eV) was smaller than the E_{CB} of LaNi_{0.6}Fe_{0.4}O₃ (−0.36 eV), while the E_{VB} of

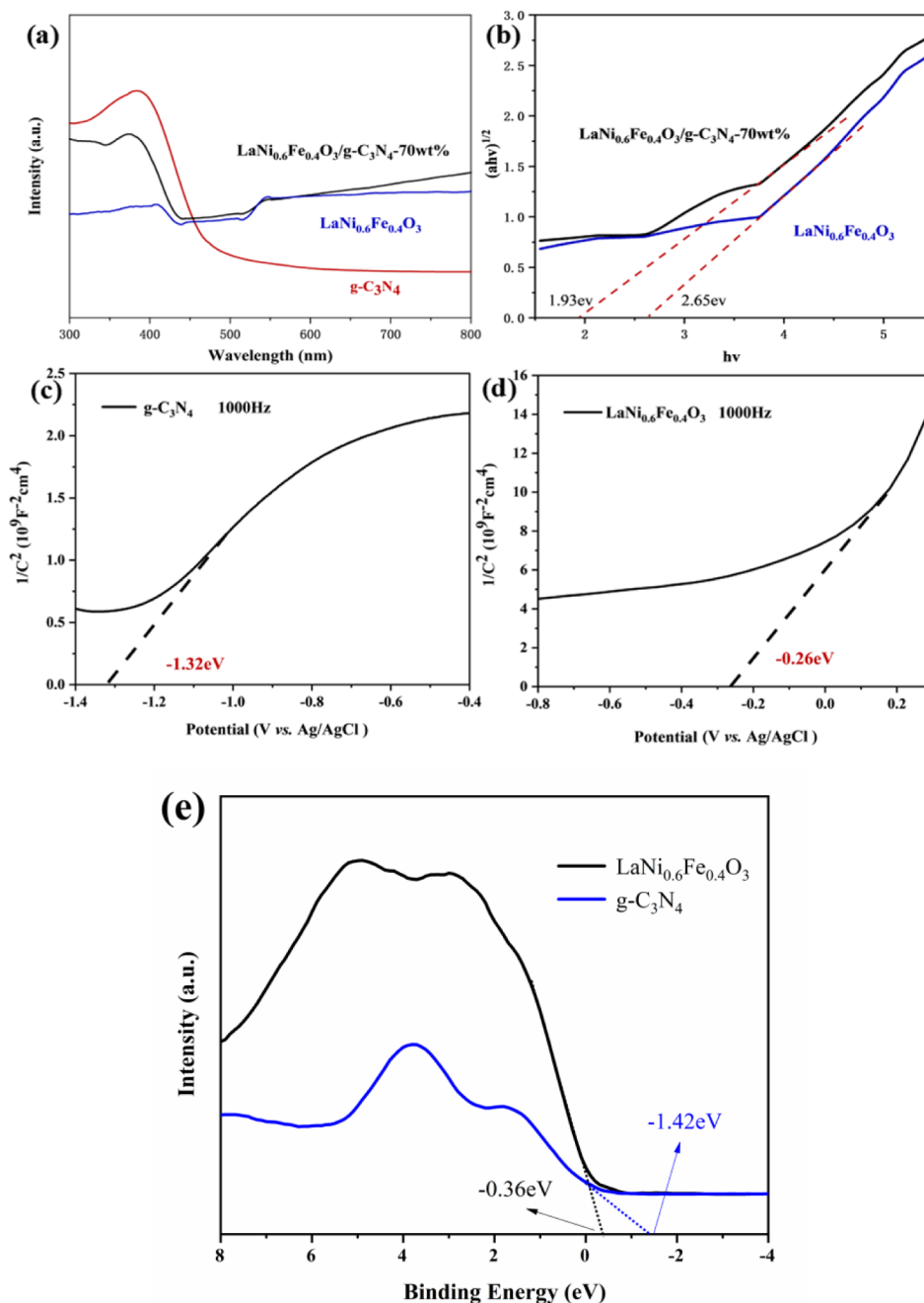


Figure 7. (a) UV-vis diffuse reflectance spectra (DRS) of LaNi_{0.6}Fe_{0.4}O₃, g-C₃N₄, and LaNi_{0.6}Fe_{0.4}O₃/g-C₃N₄; (b) the bandgap energy (E_g) diagram of LaNi_{0.6}Fe_{0.4}O₃ and LaNi_{0.6}Fe_{0.4}O₃/g-C₃N₄; (c, d) the Mott-Schottky (M-S) plots collected at 1000 Hz; and (e) the valence band (VB) XPS spectra for LaNi_{0.6}Fe_{0.4}O₃ and g-C₃N₄.

Table 3. LaNi_{0.6}Fe_{0.4}O₃ and g-C₃N₄ Bandgaps

sample	χ (eV)	E_{CB} (eV)	E_{VB} (eV)	E_g
LaNi _{0.6} Fe _{0.4} O ₃	6.60	-0.36	2.29	2.65
g-C ₃ N ₄	4.63	-1.42	1.68	3.10

LaNi_{0.6}Fe_{0.4}O₃ (2.29 eV) was larger than the E_{VB} of g-C₃N₄ (1.68 eV). The Mott-Schottky (M-S) curves for LaNi_{0.6}Fe_{0.4}O₃ and g-C₃N₄ exhibited positive slopes, indicating they are n-type semiconductors, which is consistent with reported results.³⁵ In addition, the flat band potentials (E_f) of g-C₃N₄ (-1.32 V vs Ag/AgCl) and LaNi_{0.6}Fe_{0.4}O₃ (-0.26 V vs Ag/AgCl) were obtained from Mott-Schottky (M-S) plots. Based on the voltage difference of approximately 0.1 V between the E_{CB} and E_f for

an n-type semiconductor, the E_{CB} values were calculated as -1.42 and -0.36 eV (relative to NHE) for g-C₃N₄ and LaNi_{0.6}Fe_{0.4}O₃, respectively. Therefore, this was consistent with the data obtained using the empirical formulas to calculate E_{CB} and E_{VB} . By properly constructing the LaNi_{0.6}Fe_{0.4}O₃/g-C₃N₄ heterojunction, it was possible to establish a band structure that enabled S-scheme charge transfer. When the two semiconductors come into contact with each other, the electrons in g-C₃N₄ spontaneously migrate to LaNi_{0.6}Fe_{0.4}O₃. This results in an electron depletion region and an electron accumulation region near the interface of g-C₃N₄ and LaNi_{0.6}Fe_{0.4}O₃, respectively. This results in the formation of an internal electric field from g-C₃N₄ to LaNi_{0.6}Fe_{0.4}O₃. This internal electric field

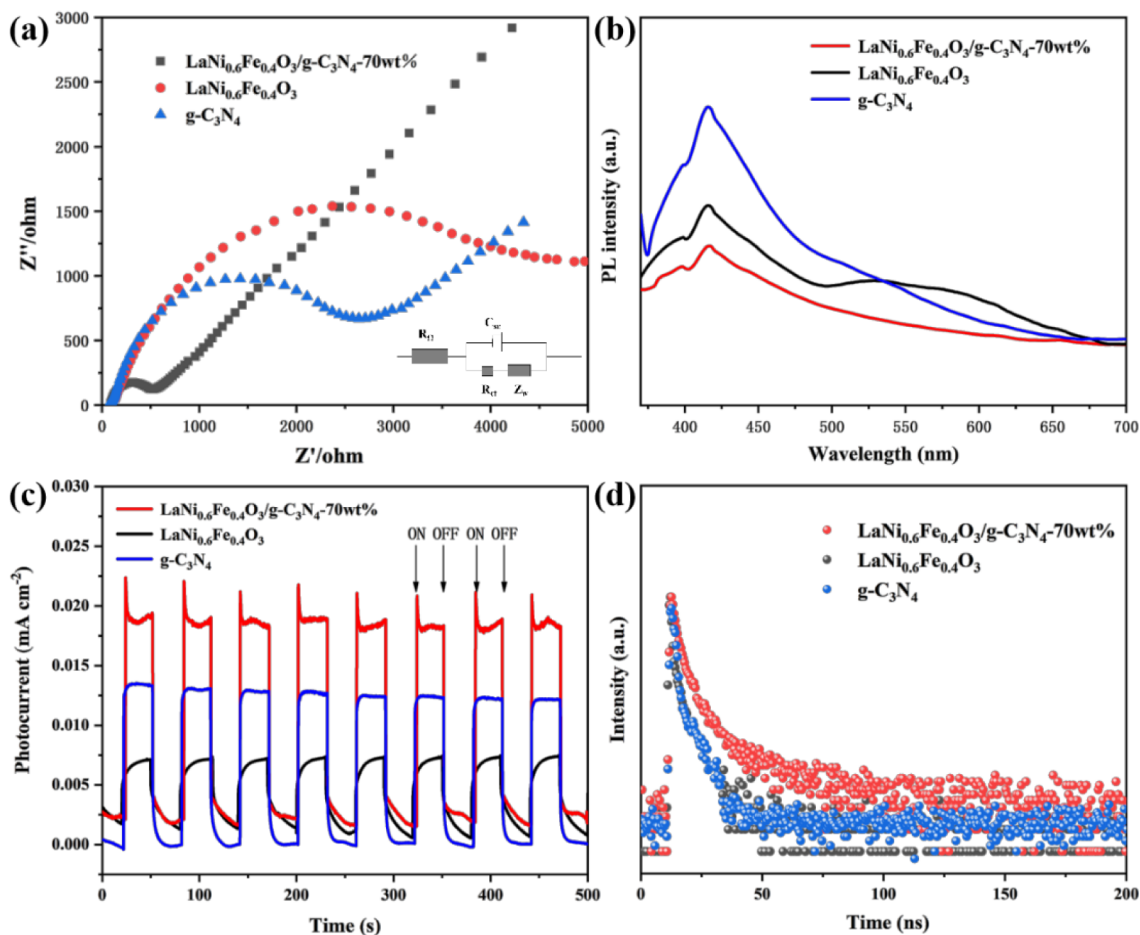


Figure 8. (a) Electrochemical impedance spectra (EIS) plot; (b) photoluminescence (PL) spectra; (c) photocurrent response spectra; (d) time-resolved fluorescence spectra of $\text{LaNi}_{0.6}\text{Fe}_{0.4}\text{O}_3$, $\text{g-C}_3\text{N}_4$, and $\text{LaNi}_{0.6}\text{Fe}_{0.4}\text{O}_3/\text{g-C}_3\text{N}_4$ -70 wt %.

accelerates the transfer of photogenerated electrons from $\text{LaNi}_{0.6}\text{Fe}_{0.4}\text{O}_3$ to $\text{g-C}_3\text{N}_4$. When two semiconductors touch each other, their Fermi energies should align to the same level. This causes the Fermi levels of the lower band and the $\text{g-C}_3\text{N}_4$ to bend up and down, respectively, prompting the photogenerated electrons in the lower CB and the holes in the $\text{g-C}_3\text{N}_4$ VB to recombine in the interface region. The Coulomb attraction between holes and electrons facilitates the recombination of photogenerated electrons in the CB of $\text{LaNi}_{0.6}\text{Fe}_{0.4}\text{O}_3$ and holes in the VB of RGO at the interface. The photogenerated electrons retained in CB of $\text{g-C}_3\text{N}_4$ and photogenerated holes in VB of $\text{LaNi}_{0.6}\text{Fe}_{0.4}\text{O}_3$ can be reduced and oxidized, respectively.

Electrochemical impedance spectroscopy was used to investigate the carrier migration resistance.³⁶ On this basis, the impedance responses were determined for the catalyst ($\text{LaNi}_{0.6}\text{Fe}_{0.4}\text{O}_3/\text{g-C}_3\text{N}_4$ -70 wt %), pure $\text{LaNi}_{0.6}\text{Fe}_{0.4}\text{O}_3$, and $\text{g-C}_3\text{N}_4$. In the impedance plots for pure $\text{g-C}_3\text{N}_4$ and pure $\text{LaNi}_{0.6}\text{Fe}_{0.4}\text{O}_3$, the intersection of the semicircular curves with the X-axis was larger than that of the composite photocatalyst. This indicates a higher resistance to charge carrier migration in the pure $\text{LaNi}_{0.6}\text{Fe}_{0.4}\text{O}_3$ and $\text{g-C}_3\text{N}_4$ samples. Conversely, the charge transfer resistance of the catalyst ($\text{LaNi}_{0.6}\text{Fe}_{0.4}\text{O}_3/\text{g-C}_3\text{N}_4$ -70 wt %) was lower than that of $\text{LaNi}_{0.6}\text{Fe}_{0.4}\text{O}_3$ and $\text{g-C}_3\text{N}_4$. Notably, the catalyst ($\text{LaNi}_{0.6}\text{Fe}_{0.4}\text{O}_3/\text{g-C}_3\text{N}_4$ -70 wt %) exhibited the lowest charge transfer resistance, as shown in Figure 8a. These results indicated that the $\text{LaNi}_{0.6}\text{Fe}_{0.4}\text{O}_3/\text{g-C}_3\text{N}_4$ -70 wt % composite photocatalyst had a higher hydrogen

production rate and more effectively suppressed the recombination of photogenerated electron–hole pairs. EIS can also prove that for the S-scheme heterojunction system, if the arc radius of the composite material is the smallest, the photocatalytic activity is the worst, indicating that the S-scheme heterojunction is conducive to reducing the charge transfer resistance and promoting the carrier separation.

The efficiency for separation and transfer of the photogenerated electrons and holes was evaluated with photoluminescence (PL) spectroscopy.³⁷ The height of the peak in the fluorescence spectrum is directly related to the recombination rate for photogenerated electrons and holes, and a higher intensity indicates a higher recombination rate.³⁸ Figure 8b shows the different results for fluorescence excitation of $\text{LaNi}_{0.6}\text{Fe}_{0.4}\text{O}_3$, $\text{g-C}_3\text{N}_4$, and the $\text{LaNi}_{0.6}\text{Fe}_{0.4}\text{O}_3/\text{g-C}_3\text{N}_4$ composite materials with 300 nm illumination. With 300 nm excitation, the fluorescence response of the $\text{LaNi}_{0.6}\text{Fe}_{0.4}\text{O}_3/\text{g-C}_3\text{N}_4$ composite material was significantly lower than that of pure $\text{g-C}_3\text{N}_4$ and pure $\text{LaNi}_{0.6}\text{Fe}_{0.4}\text{O}_3$, indicating that the fluorescence response signal of $\text{LaNi}_{0.6}\text{Fe}_{0.4}\text{O}_3/\text{g-C}_3\text{N}_4$ -70 wt % composite material is the lowest. The results also showed that the heterojunctions exhibit the lowest rate for recombination of the photogenerated electrons and holes, which enhanced the photocatalytic decomposition of water. In addition, the fluorescence band edge of the $\text{LaNi}_{0.6}\text{Fe}_{0.4}\text{O}_3/\text{g-C}_3\text{N}_4$ composite material was blue-shifted compared to that of the pure $\text{g-C}_3\text{N}_4$ composite material, indicating an electronic interaction between

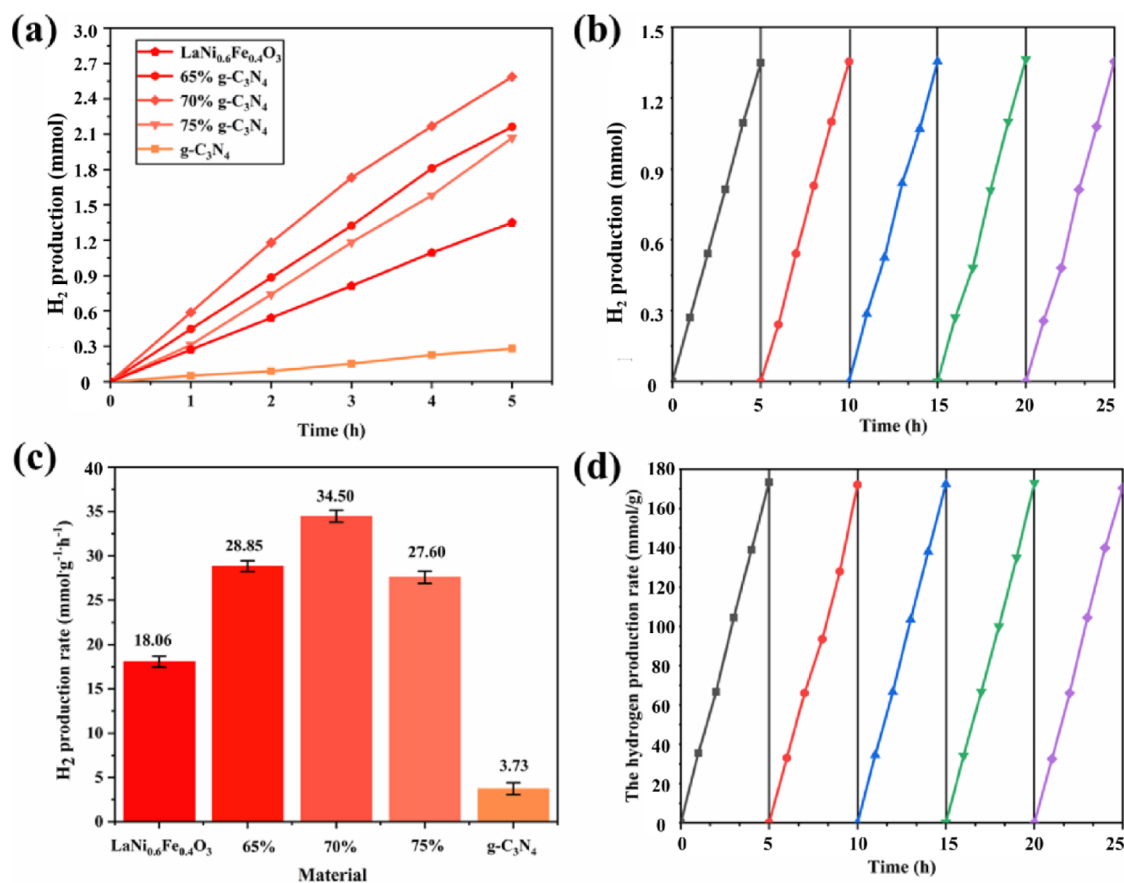


Figure 9. (a) Photocatalytic hydrogen evolution rates of LaNi_{0.6}Fe_{0.4}O₃, g-C₃N₄, and LaNi_{0.6}Fe_{0.4}O₃/g-C₃N₄-65, 70, and 75 wt % as a function of irradiation time under full spectrum illumination; (b) long-term stability test of LaNi_{0.6}Fe_{0.4}O₃ under continuous illumination; (c) average hydrogen evolution rates during water splitting by LaNi_{0.6}Fe_{0.4}O₃, g-C₃N₄, and LaNi_{0.6}Fe_{0.4}O₃/g-C₃N₄-65, 70, and 75 wt % under full illumination; (d) long-term stability test of LaNi_{0.6}Fe_{0.4}O₃/g-C₃N₄-70 wt % under continuous illumination for 25 h.

LaNi_{0.6}Fe_{0.4}O₃ and the g-C₃N₄ composite material. The photoluminescence spectrum confirmed that the recombination of the photogenerated electrons and holes in LaNi_{0.6}Fe_{0.4}O₃/g-C₃N₄ was strongly suppressed, mainly due to the migration of the photogenerated electrons in the conduction band of LaNi_{0.6}Fe_{0.4}O₃ to the valence band. The g-C₃N₄ forms an S-scheme heterojunction under full wavelength light irradiation, which effectively suppressed the direct recombination of electron–hole pairs.

The transient (on/off) photocurrent response (Figure 8c) revealed the current responses of LaNi_{0.6}Fe_{0.4}O₃, g-C₃N₄, and LaNi_{0.6}Fe_{0.4}O₃/g-C₃N₄ under illumination. Pure LaNi_{0.6}Fe_{0.4}O₃ and g-C₃N₄ exhibited relatively weak photocurrent responses under illumination. In contrast, LaNi_{0.6}Fe_{0.4}O₃/g-C₃N₄ showed a significantly stronger, faster, and stable photocurrent response. The photocurrent response remained unchanged after multiple cycles, without attenuation or time delays. The photocurrent density of the LaNi_{0.6}Fe_{0.4}O₃/g-C₃N₄ composite material was 0.018 mA·cm⁻², which was higher than that of LaNi_{0.6}Fe_{0.4}O₃ (0.012 mA·cm⁻²) and g-C₃N₄ (0.005 mA·cm⁻²), indicating the strongest transient photocurrent response. This means that it has a higher charge separation efficiency, which means that more electrons and holes can participate in the photocatalytic reaction. The photogenerated electrons diffused toward the back to form a photocurrent, and the holes were absorbed by hole receptors in the electrolyte. Therefore, the composite catalyst (LaNi_{0.6}Fe_{0.4}O₃/g-C₃N₄-70 wt %) showed highly

efficient separation of the photogenerated electron–hole pairs.³⁹

We used time-resolved fluorescence spectroscopy to determine the lifetimes of photogenerated charge carriers in the samples. The average lifespan of the sample was calculated via multiple exponential fittings, as shown in Figure 8d. The average photogenerated carrier lifetime of the LaNi_{0.6}Fe_{0.4}O₃/g-C₃N₄-70 wt % composite photocatalyst was 7.72 ns, which was significantly longer than that of LaNi_{0.6}Fe_{0.4}O₃ (4.28 ns). The longer fluorescence lifetime indicates an improvement in the charge separation efficiency, which is useful for photocatalytic reactions.

As shown in Figure 9a, hydrogen evolution was detected with gas chromatography, and the experiments were conducted in triplicate for all samples, as shown in Figure 9c, to eliminate any unexpected factors and obtain more convincing data. The heterostructure materials exhibited different hydrogen evolution rates with varying doping ratios of g-C₃N₄. Since the calculated errors were 0.02% or lower, the repeatability and reproducibility of the data were confirmed. Clearly, the prepared g-C₃N₄, LaNi_{0.6}Fe_{0.4}O₃, and LaNi_{0.6}Fe_{0.4}O₃/g-C₃N₄-65, 70, and 75 wt % composite materials exhibited varying amounts of photocatalytic hydrogen evolution, and the hydrogen evolution rates were 0.08 mmol·h⁻¹·μmol⁻¹, 0.36 mmol·h⁻¹·μmol⁻¹, 0.58 mmol·h⁻¹·μmol⁻¹, 0.39 mmol·h⁻¹·μmol⁻¹, and 0.55 mmol·h⁻¹·μmol⁻¹ (3.73 mmol·h⁻¹·g⁻¹, 18.06 mmol·h⁻¹·g⁻¹, 28.85 mmol·h⁻¹·g⁻¹, 34.50 mmol·h⁻¹·g⁻¹, and 27.60 mmol·h⁻¹·g⁻¹), respectively. LaNi_{0.6}Fe_{0.4}O₃/g-C₃N₄-70 wt % exhibited the

highest photocatalytic activity, with an average hydrogen evolution rate of $34.50 \text{ mmol}\cdot\text{h}^{-1}\cdot\text{g}^{-1}$, which was 2.0 times and 9.2 times higher than that of $\text{LaNi}_{0.6}\text{Fe}_{0.4}\text{O}_3$ and $\text{g-C}_3\text{N}_4$, respectively. Even after 5 consecutive cycles, the photocatalytic efficiency of the catalyst was not significantly decreased, indicating its high stability during the photocatalytic water splitting process under xenon lamp irradiation. Similarly, we also compared the photocatalytic activities of LaNiO_3 and $\text{LaNiO}_3/\text{g-C}_3\text{N}_4$ (Figure S5). The AQYs (apparent quantum yields) of $\text{LaNi}_{0.6}\text{Fe}_{0.4}\text{O}_3/\text{g-C}_3\text{N}_4$ -70 wt % at 300, 420, 450, 500, and 600 nm were 3.85%, 3.65%, 3.80%, 3.31%, and 3.30%, respectively, as shown in Figure 10. What's more, there was no distinct

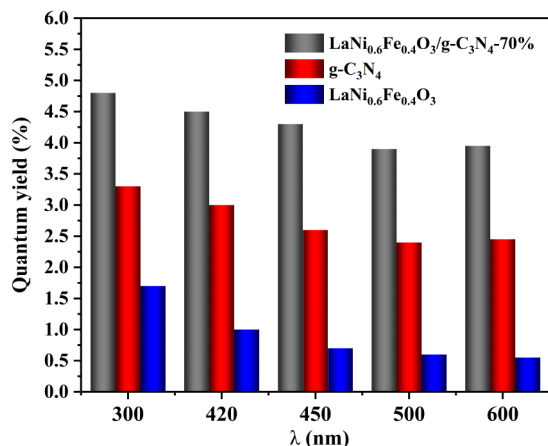


Figure 10. Apparent quantum yields of the composite materials at different wavelengths.

change in the XRD patterns and FT-IR images of $\text{LaNi}_{0.6}\text{Fe}_{0.4}\text{O}_3/\text{g-C}_3\text{N}_4$ -70 wt % before and after five cyclic photocatalytic experiments, as observed in Figure S6, respectively. The results further confirmed the former conclusion that our synthesized $\text{LaNi}_{0.6}\text{Fe}_{0.4}\text{O}_3/\text{g-C}_3\text{N}_4$ -70 wt % nanoparticles had good stability and sturdy crystal structure.

3.2. Mechanism Analysis. Electron paramagnetic resonance (EPR) spectroscopy was used to confirm the S-scheme mechanism for the $\text{LaNi}_{0.6}\text{Fe}_{0.4}\text{O}_3/\text{g-C}_3\text{N}_4$ photocatalyst, 5,5-dimethylpyrroline-*N*-oxide (DMPO) was used as a spin trap to detect the spin distribution of hydroxyl radicals ($\bullet\text{OH}$), and 5-*tert*-butoxycarbonyl-5-methyl-1-pyrroline-*N*-oxide (BMPO) was used as a spin trap to detect the spin distribution of superoxide radicals ($\bullet\text{O}_2^-$). The holes and electrons created by light successfully drive the formation of hydroxyl radicals and superoxide radicals. EPR spectroscopy provides valuable information on the presence and behavior of these free radicals, enabling an investigation of the photocatalytic mechanism.^{40,41}

The EPR spectra of $\text{BMPO}\cdot\bullet\text{O}_2^-$ and $\text{DMPO}\cdot\bullet\text{OH}$ were measured for $\text{LaNi}_{0.6}\text{Fe}_{0.4}\text{O}_3$, $\text{g-C}_3\text{N}_4$, and $\text{LaNi}_{0.6}\text{Fe}_{0.4}\text{O}_3/\text{g-C}_3\text{N}_4$ during irradiation, as shown in Figure 11a,b. The $\text{BMPO}\cdot\bullet\text{O}_2^-$ signal of $\text{LaNi}_{0.6}\text{Fe}_{0.4}\text{O}_3/\text{g-C}_3\text{N}_4$ was significantly higher than that of pure $\text{g-C}_3\text{N}_4$, while the $\text{BMPO}\cdot\bullet\text{O}_2^-$ signal for pure $\text{LaNi}_{0.6}\text{Fe}_{0.4}\text{O}_3$ was almost absent (Figure 11a). Figure 11b shows that although the $\text{DMPO}\cdot\bullet\text{OH}$ signal of the pristine $\text{g-C}_3\text{N}_4$ was very weak, the $\text{DMPO}\cdot\bullet\text{OH}$ signal of the composite photocatalyst $\text{LaNi}_{0.6}\text{Fe}_{0.4}\text{O}_3/\text{g-C}_3\text{N}_4$ was significantly stronger than that of $\text{LaNi}_{0.6}\text{Fe}_{0.4}\text{O}_3$.⁴² The relative peak intensities for the $\text{DMPO}\cdot\bullet\text{OH}$ radicals formed by $\text{LaNi}_{0.6}\text{Fe}_{0.4}\text{O}_3$ and $\text{LaNi}_{0.6}\text{Fe}_{0.4}\text{O}_3/\text{g-C}_3\text{N}_4$ exhibited ratios of 1:2:2:1. The weaker EPR signals for $\text{BMPO}\cdot\bullet\text{O}_2^-$ from the pristine $\text{LaNi}_{0.6}\text{Fe}_{0.4}\text{O}_3$

and $\text{g-C}_3\text{N}_4$ were attributed to their negative potentials relative to $\text{O}_2/\bullet\text{O}_2^-$. However, for the composite photocatalyst $\text{LaNi}_{0.6}\text{Fe}_{0.4}\text{O}_3/\text{g-C}_3\text{N}_4$, the $\text{BMPO}\cdot\bullet\text{O}_2^-$ signal was significantly stronger.⁴³ Therefore, we speculate that $\bullet\text{O}_2^-$ may have originated from the conduction band (CB) of $\text{LaNi}_{0.6}\text{Fe}_{0.4}\text{O}_3$ in the $\text{LaNi}_{0.6}\text{Fe}_{0.4}\text{O}_3/\text{g-C}_3\text{N}_4$ heterojunction, and due to the rapid consumption of the photogenerated holes in $\text{g-C}_3\text{N}_4$, it significantly enhanced the charge carrier separation efficiency. As shown in Figure 11c, no $\text{BMPO}\cdot\bullet\text{O}_2^-$ or $\text{DMPO}\cdot\bullet\text{OH}$ was observed on the catalyst surface under dark, indicating that $\bullet\text{O}_2^-$ and $\bullet\text{OH}$ were produced on the catalyst surface during illumination. We calculated a *g*-value of 2.002 for the $\text{LaNi}_{0.6}\text{Fe}_{0.4}\text{O}_3/\text{g-C}_3\text{N}_4$ -70 wt % complex, indicating the presence of oxygen vacancies in the complex, as shown in Figure 11d. Fe doping increases the presence of oxygen vacancies and inhibits the recombination of electron holes. After the formation of the heterojunction, the oxygen vacancy is also greatly increased, which will optimize the presence of the built-in electric field and promote improved performance.

Ultraviolet photoelectron spectroscopy (UPS) was used to confirm the redox potentials of $\text{LaNi}_{0.6}\text{Fe}_{0.4}\text{O}_3$ and $\text{g-C}_3\text{N}_4$, and the work functions were found to be 4.18 and 3.88 eV, respectively. As shown in Figure 12, the cutoff energies for $\text{LaNi}_{0.6}\text{Fe}_{0.4}\text{O}_3$ and $\text{g-C}_3\text{N}_4$ were 17.04 and 17.34 eV, respectively. It is evident that the Fermi level (E_f) of $\text{g-C}_3\text{N}_4$ was lower than that of the $\text{LaNi}_{0.6}\text{Fe}_{0.4}\text{O}_3$ catalyst, indicating a more negative E_f for $\text{g-C}_3\text{N}_4$. When $\text{LaNi}_{0.6}\text{Fe}_{0.4}\text{O}_3$ came into contact with $\text{g-C}_3\text{N}_4$, photoexcited electrons from $\text{g-C}_3\text{N}_4$ migrated to $\text{LaNi}_{0.6}\text{Fe}_{0.4}\text{O}_3$ until their Fermi levels aligned, resulting in a built-in electric field generated at the interface. This built-in electric field separated the electron-hole pairs and suppressed recombination, thereby enhancing the photocatalytic activity. This led to an increase in the electron density on the surface of $\text{LaNi}_{0.6}\text{Fe}_{0.4}\text{O}_3$ and a decrease in the electron density on the surface of the $\text{g-C}_3\text{N}_4$. The built-in electric field generated at the interface between $\text{LaNi}_{0.6}\text{Fe}_{0.4}\text{O}_3$ and $\text{g-C}_3\text{N}_4$ separated the electron-hole pairs with strong redox potentials. The valence band (E_{VB}) energies calculated for $\text{g-C}_3\text{N}_4$ and $\text{LaNi}_{0.6}\text{Fe}_{0.4}\text{O}_3$ were 6.18 and 6.79 eV, respectively (Table 3). Consequently, the E_{VB} values for $\text{g-C}_3\text{N}_4$ and $\text{LaNi}_{0.6}\text{Fe}_{0.4}\text{O}_3$ were 1.68 and 2.29 eV, respectively, relative to the reversible hydrogen electrode (RHE). The conduction band (E_{CB}) energies were -1.42 and -0.36 eV for $\text{g-C}_3\text{N}_4$ and $\text{LaNi}_{0.6}\text{Fe}_{0.4}\text{O}_3$, respectively. These results indicated that the S-scheme nanoheterojunction between $\text{LaNi}_{0.6}\text{Fe}_{0.4}\text{O}_3$ and $\text{g-C}_3\text{N}_4$ was formed because their band structures were aligned. This was attributed to the higher electron energy distribution and increased electron density on the surface of $\text{LaNi}_{0.6}\text{Fe}_{0.4}\text{O}_3$, while the electron energy distribution on the surface of $\text{g-C}_3\text{N}_4$ was lower, which was consistent with the XPS results. Figure 12 presents the band structures of $\text{g-C}_3\text{N}_4$ and $\text{LaNi}_{0.6}\text{Fe}_{0.4}\text{O}_3$ obtained from the UPS spectra, which confirmed their strong binding. This was consistent with the XPS analysis results, as well. The successful construction of the S-scheme heterojunction enabled efficient charge separation and transfer, thereby enhancing the photocatalytic hydrogen evolution.

Based on the analyses and results presented above, a mechanism was developed for photocatalytic hydrogen evolution with $\text{LaNi}_{0.6}\text{Fe}_{0.4}\text{O}_3/\text{g-C}_3\text{N}_4$. As shown in Figure 13, $\text{LaNi}_{0.6}\text{Fe}_{0.4}\text{O}_3$ and $\text{g-C}_3\text{N}_4$ had well-matched band structures, indicating an S-scheme staggered n-n heterojunction. As depicted in Figure 13a, prior to the contact between the two phases, $\text{LaNi}_{0.6}\text{Fe}_{0.4}\text{O}_3$ exhibited a lower E_f energy level and band

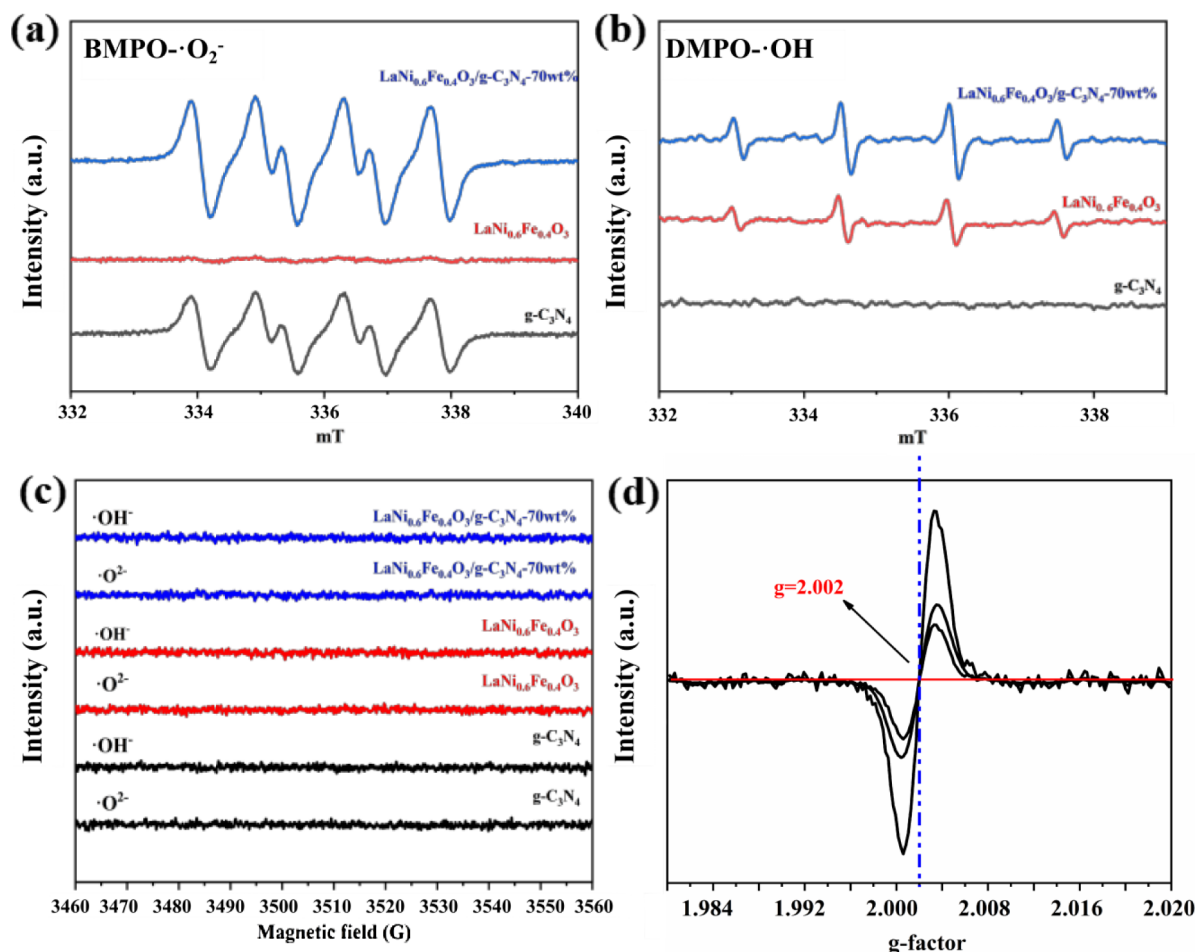
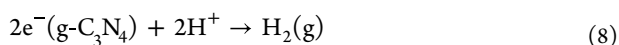
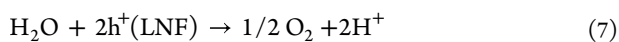
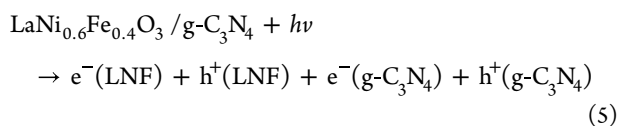


Figure 11. (a) Water dispersion of BMPO-•O₂⁻ and (b) water dispersion of DMPO-•OH under full spectrum xenon lamp irradiation; (c) EPR spectra and (d) g-values of LaNiO₃, LaNi_{0.6}Fe_{0.4}O₃, and LaNi_{0.6}Fe_{0.4}O₃/g-C₃N₄-70 wt % composites from the bottom up.

position than g-C₃N₄. Therefore, when LaNi_{0.6}Fe_{0.4}O₃ was in close proximity to g-C₃N₄, the free electrons within g-C₃N₄ were spontaneously transferred to LaNi_{0.6}Fe_{0.4}O₃ through the interface until their E_f energy levels aligned precisely. This resulted in the formation of an S-scheme heterojunction, enabling efficient charge separation and transfer, as illustrated in Figure 13c.

If it is a type II heterojunction, the hole of LaNi_{0.6}Fe_{0.4}O₃ will transfer to g-C₃N₄ to generate the •OH radical, and its peak value should be the highest. However, the fact that LaNi_{0.6}Fe_{0.4}O₃/g-C₃N₄ has the strongest DMPO-•OH signal indicates that the heterojunction retains the high oxidation capacity of the holes in LaNi_{0.6}Fe_{0.4}O₃ and inhibits electron–hole recombination. This result proves that LaNi_{0.6}Fe_{0.4}O₃/g-C₃N₄ is an S-scheme heterojunction rather than a type II heterojunction. The specific photocatalytic process was as follows:



In this process, the strongly reducing electrons remained in the conduction band (CB) of LaNi_{0.6}Fe_{0.4}O₃ and provided a strong driving force for the reduction of protons (H⁺) to H₂ in water. The valence band (VB) position of g-C₃N₄ retains strongly oxidizing holes, which were consumed by protons (H⁺) in the water containing the sacrificial agent CH₃OH. The LaNi_{0.6}Fe_{0.4}O₃/g-C₃N₄ composite material exhibited a high efficiency for the separation of photoexcited electron–hole pairs due to the availability of fast charge transfer pathways. The S-scheme heterojunction enhanced the close contact between LaNi_{0.6}Fe_{0.4}O₃ and g-C₃N₄, exposed more active sites, and promoted the evolution of H₂. Therefore, the thin film nanostructure increased the active surface area of the photocatalyst, thereby shortening the diffusion distance of the charge carriers. This increased the charge transfer rate and enhanced the performance of photocatalytic water splitting for H₂ production.

4. CONCLUSION

The Fe-doped LaNi_{0.6}Fe_{0.4}O₃/g-C₃N₄ S-scheme nanoheterojunction composite photocatalyst was prepared via the sol–gel method. It exhibited a high density of active sites, efficient charge separation, and abundant oxygen vacancy. While the oxygen vacancy provides more photogenerated charge carriers, the 2D/2D structure enhances the bonding of the heterojunction, generating an inherent electric field and promoting the separation of e⁻ and h⁺. Based on the capture test (EPR) of •OH

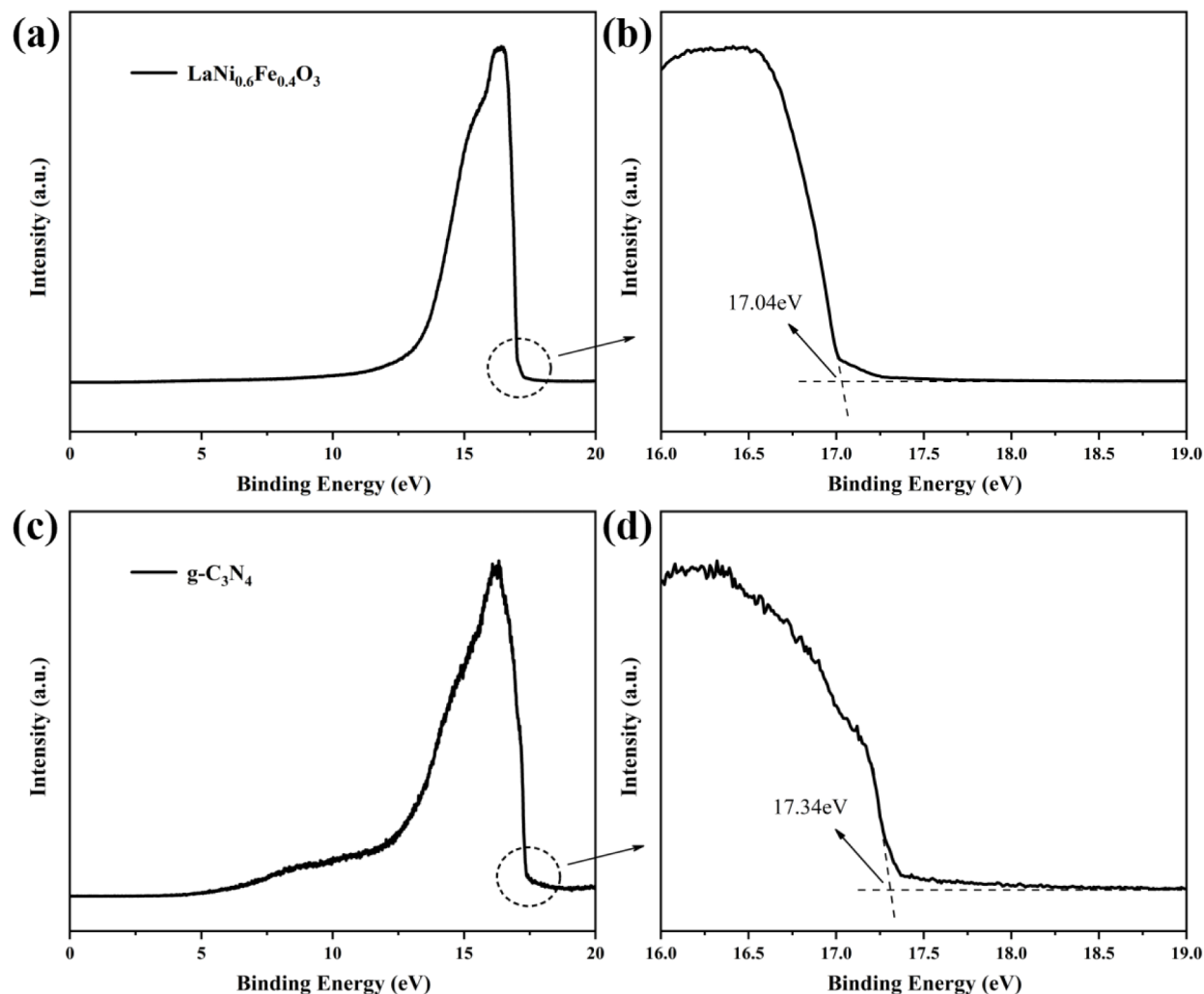


Figure 12. Ultraviolet photoelectron spectra (UPS) of (a,b) $\text{LaNi}_{0.6}\text{Fe}_{0.4}\text{O}_3$ and (c,d) $\text{g-C}_3\text{N}_4$.

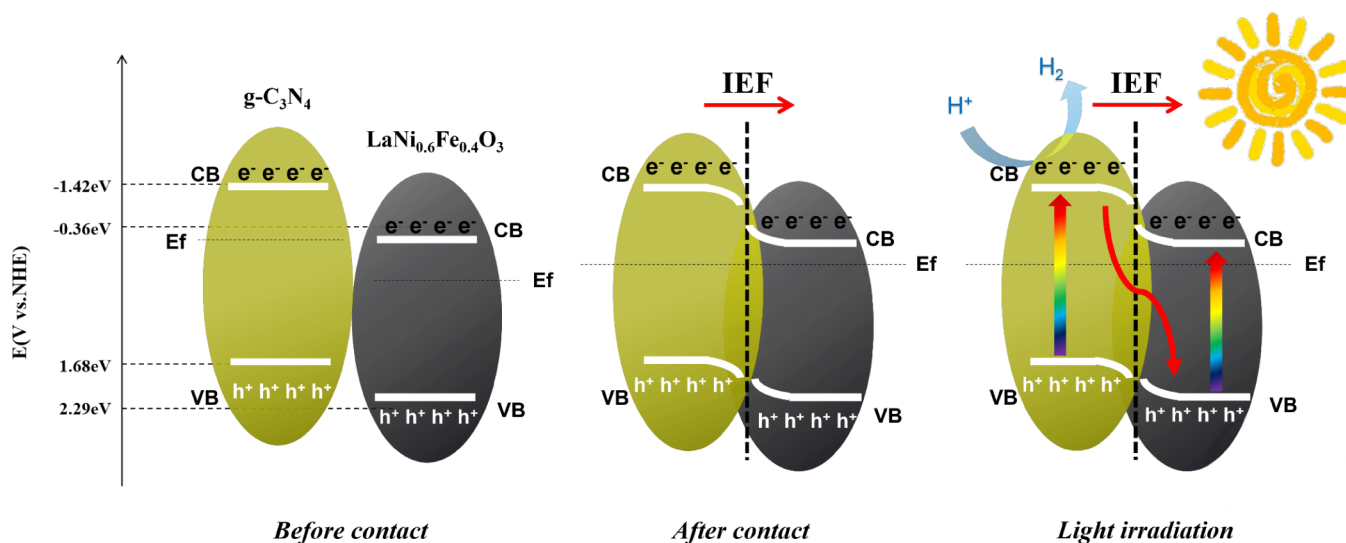


Figure 13. Schematic band diagrams for $\text{LaNi}_{0.6}\text{Fe}_{0.4}\text{O}_3$ and $\text{g-C}_3\text{N}_4$ (a) before contact, (b) after contact, and (c) charge transfer across the S-scheme heterojunction of $\text{LaNi}_{0.6}\text{Fe}_{0.4}\text{O}_3/\text{g-C}_3\text{N}_4$ during the reaction.

free radicals, it can be seen that the enhanced activity is attributed to the S-scheme carrier migration mechanism in the heterojunction, which promotes the rapid adsorption of H^+ by

the abundant amino sites in $\text{g-C}_3\text{N}_4$, thus effectively generating H_2 . The presence of the Fe dopant was confirmed by the XRD and EDS spectra. The chemical states of the elements in the

photocatalyst were determined with X-ray photoelectron spectroscopy (XPS). Structural characterization with SEM and TEM revealed that the $\text{LaNi}_{0.6}\text{Fe}_{0.4}\text{O}_3$ nanoparticles measured approximately 60 nm and exhibited spherical shapes, while $\text{g-C}_3\text{N}_4$ had a layered structure with a consistent morphology. $\text{LaNi}_{0.6}\text{Fe}_{0.4}\text{O}_3$ composite nanoparticles and $\text{g-C}_3\text{N}_4$ nanosheets were observed, and the composite material was highly hydrophilic. During irradiation, the maximum photocatalytic activity of $\text{LaNi}_{0.6}\text{Fe}_{0.4}\text{O}_3$ was $18.06 \text{ mmol}\cdot\text{h}^{-1}\cdot\text{g}^{-1}$, which was 21.2 times higher than that of LaNiO_3 . Moreover, the highest photocatalytic activity of the $\text{LaNi}_{0.6}\text{Fe}_{0.4}\text{O}_3/\text{g-C}_3\text{N}_4$ -70 wt % was $34.50 \text{ mmol}\cdot\text{h}^{-1}\cdot\text{g}^{-1}$, which was 40.6 times higher than that of LaNiO_3 and 9.2 times higher than that of $\text{g-C}_3\text{N}_4$. The photocatalytic activity of $\text{LaNi}_{0.6}\text{Fe}_{0.4}\text{O}_3/\text{g-C}_3\text{N}_4$ -70 wt % was significantly higher than that of other catalysts.^{27,28,44} This study demonstrated an inexpensive and highly efficient $\text{LaNi}_{0.6}\text{Fe}_{0.4}\text{O}_3/\text{g-C}_3\text{N}_4$ photocatalytic system, which utilizes a built-in electric field at the interface to promote charge separation, thereby facilitating the photocatalytic production of H_2 . These findings can be applied to water splitting and other photocatalytic processes and provide insight into the development of novel S-scheme photocatalytic materials.

■ ASSOCIATED CONTENT

Data Availability Statement

All data generated or analyzed during this study are included in this published article.

Supporting Information

The Supporting Information is available free of charge at <https://pubs.acs.org/doi/10.1021/acsomega.4c02333>.

Fabrication procedure of the $\text{LaNi}_{0.6}\text{Fe}_{0.4}\text{O}_3/\text{g-C}_3\text{N}_4$ S-scheme heterojunctions; TGA, BET surface area, and BJH pore size distribution analysis; comparison and summary of other photocatalyst systems for photocatalytic H_2 evolution; and all data generated or analyzed during this study (PDF)

■ AUTHOR INFORMATION

Corresponding Authors

Xin Zhong – Department of Chemistry, Faculty of Arts and Sciences, Beijing Normal University, Zhuhai 519087, China; Email: zhongxin@bnu.edu.cn

Fubin Jiang – College of Chemistry, Beijing Normal University, Beijing 100875, China; Department of Chemistry, Faculty of Arts and Sciences, Beijing Normal University, Zhuhai 519087, China; orcid.org/0000-0003-2120-2827; Phone: +86 01058802850; Email: jfb@bnu.edu.cn

Authors

Kexin Zhang – College of Chemistry, Beijing Normal University, Beijing 100875, China; orcid.org/0009-0002-5523-2477

Rui Wang – College of Chemistry, Beijing Normal University, Beijing 100875, China; Institute of Chemical Engineering and Technology, Xi'an Jiao Tong University, Xi'an 710049, China

Complete contact information is available at:

<https://pubs.acs.org/doi/10.1021/acsomega.4c02333>

Author Contributions

K.Z. was the main author of the work, designed the project, wrote the manuscript draft, performed syntheses, used electron microscopy techniques, and coordinated all characterization and catalytic studies. R.W. was responsible for part of the synthesis

work. F.J. and X.Z. assisted with the initial draft (including substantive translation). All authors read and approved the final manuscript.

Notes

The authors declare no competing financial interest.

■ ACKNOWLEDGMENTS

This work was funded by the Beijing Normal University.

■ REFERENCES

- (1) Zhou, P.; Chen, H.; Chao, Y.; Zhang, Q.; Zhang, W.; Lv, F.; Gu, L.; Zhao, Q.; Wang, N.; Wang, J.; Guo, S. Single-atom pt-*i*3 sites on all-inorganic Cs_2SnI_6 perovskite for efficient photocatalytic hydrogen production. *Nat. Commun.* **2021**, *12* (1), 4412.
- (2) Dai, M.; He, Z.; Zhang, P.; Li, X.; Wang, S. ZnWO_4 - ZnIn_2S_4 S-scheme heterojunction for enhanced photocatalytic H_2 evolution. *J. Mater. Sci. Technol.* **2022**, *122*, 231–242.
- (3) Xi, Y.; Chen, W.; Dong, W.; Fan, Z.; Wang, K.; Shen, Y.; Tu, G.; Zhong, S.; Bai, S. Engineering an interfacial facet of S-scheme heterojunction for improved photocatalytic hydrogen evolution by modulating the internal electric field. *ACS Appl. Mater. Interfaces* **2021**, *13* (33), 39491–39500.
- (4) Wu, Y.; Sakurai, T.; Adachi, T.; Wang, Q. Alternatives to water oxidation in the photocatalytic water splitting reaction for solar hydrogen production. *Nanoscale* **2023**, *15* (14), 6521–6535.
- (5) Cheng, C.; He, B.; Fan, J.; Cheng, B.; Cao, S.; Yu, J. An inorganic/organic S-scheme heterojunction H_2 -production photocatalyst and its charge transfer mechanism. *Adv. Mater.* **2021**, *33* (22), 2100317.
- (6) He, F.; Zhu, B.; Cheng, B.; Yu, J.; Ho, W.; Macyk, W. 2D/2D/0D $\text{TiO}_2/\text{C}_3\text{N}_4/\text{Ti}_3\text{C}_2$ mxene composite S-scheme photocatalyst with enhanced CO_2 reduction activity. *Appl. Catal., B* **2020**, *272*, 119006.
- (7) Li, X.; Wu, X.; Liu, S.; Li, Y.; Fan, J.; Lv, K. Effects of fluorine on photocatalysis. *Chin. J. Catal.* **2020**, *41* (10), 1451–1467.
- (8) He, Z.; Zhang, J.; Li, X.; Guan, S.; Dai, M.; Wang, S. 1D/2D heterostructured photocatalysts: from design and unique properties to their environmental applications. *Small* **2020**, *16* (46), 2005051.
- (9) Qin, J.; Lin, L.; Wang, X. A perovskite oxide LaCoO_3 cocatalyst for efficient photocatalytic reduction of CO_2 with visible light. *Chem. Commun.* **2018**, *54* (18), 2272–2275.
- (10) Zhang, G.; Liu, G.; Wang, L.; Irvine, J. T. Inorganic perovskite photocatalysts for solar energy utilization. *Chem. Soc. Rev.* **2016**, *45* (21), 5951–5984.
- (11) Khettab, M.; Omeiri, S.; Sellam, D.; Ladjouzi, M. A.; Trari, M. Characterization of LaNiO_3 prepared by sol-gel: application to hydrogen evolution under visible light. *Mater. Chem. Phys.* **2012**, *132* (2–3), 625–630.
- (12) Li, Y.; Yao, S.; Wen, W.; Xue, L.; Yan, Y. Sol-gel combustion synthesis and visible-light-driven photocatalytic property of perovskite LaNiO_3 . *J. Alloy. Compd.* **2010**, *491* (1–2), 560–564.
- (13) Ye, C.; Wang, R.; Wang, H.; Jiang, F. The high photocatalytic efficiency and stability of $\text{LaNiO}_3/\text{g-C}_3\text{N}_4$ heterojunction nanocomposites for photocatalytic water splitting to hydrogen. *BMC Chem.* **2020**, *14* (1), 65.
- (14) Nakhaei Pour, A.; Mousavi, M. Combined reforming of methane by carbon dioxide and water: particle size effect of Ni-Mg nanoparticles. *Int. J. Hydrog. Energy* **2015**, *40* (38), 12985–12992.
- (15) Nakhaei Pour, A.; Hosaini, E.; Feyzi, M. Prediction of cobalt particle size during catalyst deactivation in fischer-tropsch synthesis. *J. Iran. Chem. Soc.* **2016**, *13* (1), 139–147.
- (16) Bian, Z.; Das, S.; Wai, M. H.; Hongmanor, P.; Kawi, S. A review on bimetallic nickel-based catalysts for CO_2 reforming of methane. *ChemPhysChem* **2017**, *18* (22), 3117–3134.
- (17) Kawi, S.; Kathiraser, Y.; Ni, J.; Oemar, U.; Li, Z.; Saw, E. T. Progress in synthesis of highly active and stable nickel-based catalysts for carbon dioxide reforming of methane. *ChemSuschem* **2015**, *8* (21), 3556–3575.
- (18) Bevilacqua, M.; Montini, T.; Tavagnacco, C.; Fonda, E.; Fornasiero, P.; Graziani, M. Preparation, characterization, and

electrochemical properties of pure and composite $\text{LaNi}_{0.6}\text{Fe}_{0.4}\text{O}_3$ -based cathodes for it-sofc. *Chem. Mater.* **2007**, *19* (24), 5926–5936.

(19) Chiba, R.; Yoshimura, F.; Sakurai, Y. Investigation of $\text{LaNi}_{1-x}\text{Fe}_x\text{O}_3$ as a cathode material for solid oxide fuel cells. *Solid State Ion.* **1999**, *124* (3), 281–288.

(20) Morán-Ruiz, A.; Vidal, K.; Laguna-Bercero, M. Á.; Larrañaga, A.; Arriortua, M. I. Effects of using $(\text{La}_{0.8}\text{Sr}_{0.2})_{0.95}\text{Fe}_{0.6}\text{Mn}_{0.3}\text{Co}_{0.1}\text{O}_3$ (LSFMC), $\text{LaNi}_{0.6}\text{Fe}_{0.4}\text{O}_{3-\delta}$ (LNF) and $\text{LaNi}_{0.6}\text{Co}_{0.4}\text{O}_{3-\delta}$ (LNC) as contact materials on solid oxide fuel cells. *J. Power Sources* **2014**, *248*, 1067–1076.

(21) Morán-Ruiz, A.; Vidal, K.; Larrañaga, A.; Arriortua, M. I. Chemical compatibility and electrical contact of $\text{La-Ni}_{0.6}\text{Co}_{0.4}\text{O}_{3-\delta}$ (LNC) between $\text{CrOFeR}_{22}\text{APu}$ interconnect and $\text{La}_{0.6}\text{Sr}_{0.4}\text{FeO}_3$ (LSF) cathode for it-sofc. *Fuel Cells* **2013**, *13* (3), 398–403.

(22) Wang, L.; Si, W.; Tong, Y.; Hou, F.; Pergolesi, D.; Hou, J.; Lipper, T. T.; Dou, S.; Liang, J. Graphitic carbon nitride ($\text{g-C}_3\text{N}_4$)-based nanosized heteroarrays: Promising materials for photoelectrochemical water splitting. *Carbon Energy* **2020**, *2*, 223–250.

(23) Wang, Q.; Zhang, G.; Xing, W.; Pan, Z.; Zheng, D.; Wang, S.; Hou, Y.; Wang, X. Bottom-up Synthesis of Single-Crystalline Poly (Triazine Imide) Nanosheets for Photocatalytic Overall Water Splitting. *Angew. Chem., Int. Ed.* **2023**, *62*, No. e202307930.

(24) Chang, M.; Pan, Z.; Zheng, D.; Wang, S.; Zhang, G.; Anpo, M.; Wang, X. Salt-Melt Synthesis of Poly Heptazine Imides with Enhanced Optical Absorption for Photocatalytic Hydrogen Production. *ChemSuschem* **2023**, *16*, No. e202202255.

(25) Liu, M.; Zhang, G.; Liang, X.; Pan, Z.; Zheng, D.; Wang, S.; Yu, Z.; Hou, Y.; Wang, X. Rh/Cr₂O₃ and CoO_x Cocatalysts for Efficient Photocatalytic Water Splitting by Poly (Triazine Imide) Crystals. *Angew. Chem., Int. Ed.* **2023**, *62*, No. e202304694.

(26) Zhang, J.; Ye, G.; Zhang, C.; Pan, Z.; Wang, S.; Zhang, G.; Wang, X. Heptazine-Based Ordered-Distorted Copolymers with Enhanced Visible-Light Absorption for Photocatalytic Hydrogen Production. *ChemSuschem* **2022**, *15*, No. e202201616.

(27) Zhang, K.; Wang, R.; Jiang, F. Fe-doped metal complex ($\text{LaCo}_{0.9}\text{Fe}_{0.1}\text{O}_3$) and $\text{g-C}_3\text{N}_4$ formed a nanoheterojunction for the photocatalytic decomposition of water. *ACS Omega* **2023**, *8*, 18090.

(28) Wang, R.; Ye, C.; Wang, H.; Jiang, F. Z-scheme $\text{LaCoO}_3/\text{g-C}_3\text{N}_4$ for efficient full-spectrum light-simulated solar photocatalytic hydrogen generation. *ACS Omega* **2020**, *5* (47), 30373–30382.

(29) Deng, A.; Sun, Y.; Gao, Z.; Yang, S.; Liu, Y.; He, H.; Zhang, J.; Liu, S.; Sun, H.; Wang, S. Internal electric field in carbon nitride-based heterojunctions for photocatalysis. *Nano Energy* **2023**, *108*, 108228.

(30) Zheng, D.; Wei, G.; Xu, L.; Guo, Q.; Hu, J.; Sha, N.; Zhao, Z. $\text{LaNiFe}_{1-x}\text{O}_3$ ($0 \leq x \leq 1$) as photothermal catalysts for hydrocarbon fuels production from CO_2 and H_2O . *J. Photochem. Photobiol., A* **2019**, *377*, 182–189.

(31) Li, Y.; Liu, Y.; Wang, J.; Guo, Y.; Chu, K. Plasma-engineered nio nanosheets with enriched oxygen vacancies for enhanced electrocatalytic nitrogen fixation. *Inorg. Chem. Front.* **2020**, *7* (2), 455–463.

(32) Biju, V.; Abdul Khadar, M. Electronic structure of nanostructured nickel oxide using ni 2p xps analysis. *J. Nanopart. Res.* **2002**, *4* (3), 247.

(33) Bagus, P. S.; Nelin, C. J.; Brundle, C. R.; Crist, B. V.; Ilton, E. S.; Lahiri, N.; Rosso, K. M. Main and satellite features in the ni 2p XPS of NiO. *Inorg. Chem.* **2022**, *61* (45), 18077–18094.

(34) Dacquain, J. P.; Lancelot, C.; Dujardin, C.; Da Costa, P.; Djega-Mariadassou, G.; Beaunier, P.; Kaliaguine, S.; Vaudreuil, S.; Royer, S.; Granger, P. Influence of preparation methods of LaCoO_3 on the catalytic performances in the decomposition of N_2O . *Appl. Catal., B* **2009**, *91* (3–4), 596–604.

(35) Zheng, J.; Lei, Z. Incorporation of coo nanoparticles in 3D marigold flower-like hierarchical architecture MnCo_2O_4 for highly boosting solar light photo-oxidation and reduction ability. *Appl. Catal., B* **2018**, *237*, 1–8.

(36) Xia, J.; Di, J.; Li, H.; Xu, H.; Li, H.; Guo, S. Ionic liquid-induced strategy for carbon quantum dots/biox ($x = \text{br}, \text{cl}$) hybrid nanosheets with superior visible light-driven photocatalysis. *Appl. Catal., B* **2016**, *181*, 260–269.

(37) Yang, L.; Huang, J.; Shi, L.; Cao, L.; Yu, Q.; Jie, Y.; Fei, J.; Ouyang, H.; Ye, J. A surface modification resultant thermally oxidized porous $\text{g-C}_3\text{N}_4$ with enhanced photocatalytic hydrogen production. *Appl. Catal., B* **2017**, *204*, 335–345.

(38) Zhu, X.; Zhang, F.; Wang, M.; Ding, J.; Sun, S.; Bao, J.; Gao, C. Facile synthesis, structure and visible light photocatalytic activity of recyclable $\text{ZnFe}_2\text{O}_4/\text{TiO}_2$. *Appl. Surf. Sci.* **2014**, *319*, 83–89.

(39) Mi, Y.; Wen, L.; Wang, Z.; Cao, D.; Xu, R.; Fang, Y.; Zhou, Y.; Lei, Y. Fe(III) modified biocl ultrathin nanosheet towards high-efficient visible-light photocatalyst. *Nano Energy* **2016**, *30*, 109–117.

(40) Sayed, M.; Zhu, B.; Kuang, P.; Liu, X.; Cheng, B.; Ghamdi, A. A. A.; Wageh, S.; Zhang, L.; Yu, J. Epr investigation on electron transfer of 2D/3D $\text{g-C}_3\text{N}_4/\text{ZnO}$ S-scheme heterojunction for enhanced CO_2 photoreduction. *Adv. Sustain. Syst.* **2022**, *6* (1), 2100264.

(41) Bai, J.; Shen, R.; Chen, W.; et al. Enhanced photocatalytic H_2 evolution based on a $\text{Ti}_3\text{C}_2/\text{Zn}_{0.7}\text{Cd}_{0.3}\text{S}/\text{Fe}_2\text{O}_3$ Ohmic/S-scheme hybrid heterojunction with cascade 2D coupling interfaces. *Chem. Eng. J.* **2022**, *429*, 132587.

(42) Wang, L.; Cheng, B.; Zhang, L.; Yu, J. In situ irradiated xps investigation on S-scheme $\text{TiO}_2/\text{ZnIn}_2\text{S}_4$ photocatalyst for efficient photocatalytic CO_2 reduction. *Small* **2021**, *17* (41), 2103447.

(43) Yang, W.; Ma, G.; Fu, Y.; Peng, K.; Yang, H.; Zhan, X.; Yang, W.; Wang, L.; Hou, H. Rationally designed Ti_3C_2 mxene@ $\text{TiO}_2/\text{CuInS}_2$ schottky/S-scheme integrated heterojunction for enhanced photocatalytic hydrogen evolution. *Chem. Eng. J.* **2022**, *429*, 132381.

(44) Wang, R.; Zhang, H.; Zhong, X.; Jiang, F. Z-scheme $\text{LaCoO}_3/\text{C}_3\text{N}_4$ for efficient full-spectrum light-simulated solar photocatalytic hydrogen generation. *RSC Adv.* **2022**, *12* (37), 24026–24036.